Journal of Applied Physics ARTICLE pubs.aip.org/aip/jap

Ballistic contributions to mesoscale thermal conductivity: Closing a flux-based model with lattice–Boltzmann–Peierls–Callaway simulations

Cite as: J. Appl. Phys. **140**, 045103 (2026); doi: 10.1063/5.0332327
Submitted: 3 March 2026 · Accepted: 3 July 2026 ·
Published Online: 27 July 2026

P. Biswas,[1] J. Lee,[2] A. Roy,[2] and B. Cukurel[1,a)]

AFFILIATIONS

[1]Turbomachinery and Heat Transfer Laboratory, Faculty of Aerospace Engineering, Technion–IIT, Haifa 3200003, Israel
[2]Materials and Manufacturing Directorate, Air Force Research Laboratory, Wright–Patterson Air Force Base (WPAFB), Dayton, Ohio 45433, USA

[a)]**Author to whom correspondence should be addressed:** beni@cukurel.org. **Tel.** +972-77-887-2807

ABSTRACT

The thermal transport in dielectric and semiconductor solids departs from classical diffusion when characteristic dimensions approach phonon scattering lengths, producing mixed ballistic–diffusive behavior. Although effective conductivity is often correlated with the Knudsen number (the ratio of scattering length to sample size), such formulations do not uniquely capture phonon backscattering or provide a consistent definition for reformulating bulk properties outside the diffusive infinite sample size limit. In the scope of this work, (i) the McKelvey–Shockley Flux Method (MSFM) is extended to decompose heat flux into ballistic and diffusive contributions, and (ii) a mesoscale thermal law is derived to explicitly relate the effective thermal conductivity with ballistic thermal conductance, Knudsen number, effective backscattering length, and bulk-like thermal conductivity. To identify the latter two parameters, we perform systematic steady-state numerical experiments using a D3Q19 Lattice–Boltzmann–Peierls–Callaway (LBPC) model with separate relaxation channels for normal and Umklapp scattering. From LBPC solutions, we extract an effective phonon mean free path (equivalent to backscattering length) and a bulk-like thermal conductivity from thickness sweep regressions and use them to close the MSFM-based constitutive relations. These LBPC-extracted closure parameters are validated against existing theoretical modeling frameworks, as well as experimental data from the literature on a range of different materials. The findings reflect quantitative consistency between MSFM and LBPC as independent descriptors of ballistic–diffusive phonon transport, providing an opportunity to reduce the degrees of freedom in the model. This self-consistent mesoscale description links microscopic scattering to macroscopic behavior and supports incorporating ballistic effects into continuum models relevant to ultrafast heating, thermoelectrics, nanoelectronics, thermophones, and nanoscale information storage.

I. INTRODUCTION

Thermal transport in dielectric and semiconductor solids is governed by phonons whose mean free paths (MFPs) can span from nanometers to several micrometers, depending on dispersion,[1–4] material purity, and temperature.[5–13] When a characteristic system dimension becomes comparable to these MFPs, heat transfer departs from classical diffusion and enters a regime of partial ballistic propagation.[14–19] This transition is often characterized using the thermal *Knudsen* number, Kn, defined as the ratio of a representative phonon scattering length to a characteristic system length.[16–19] While Kn provides a useful measure of non-diffusive effects, it alone cannot capture the combined influence of geometry, boundary scattering, and the concurrent action of normal (N) and Umklapp (U) phonon scattering processes that govern mesoscale heat transport.[11–13]

This gap becomes most evident in two complementary scaling scenarios—nanoscale structures where local equilibrium fails, and macroscale samples of long MFP that remain inherently non-diffusive. For conventional materials such as silicon, germanium, and insulating dielectrics, reducing characteristic dimensions to the nanometer scale leads to a breakdown of local thermal

equilibrium. As a result, strong size effects arise, including apparent reductions in thermal conductivity and the emergence of boundary temperature discontinuities.[7,9,20–22] Classical continuum descriptions such as *Fourier*'s law,[23] the *Cattaneo–Vernotte* (CV) equation,[24,25] the dual-phase-lag (DPL) model,[26] and the *Guyer–Krumhansl* (GK) formulation[27,28] rely on local or near-equilibrium assumptions. Although these models successfully describe the behavior in bulk limits, they do not provide a unified representation of ballistic, hydrodynamic, and diffusive transport in the mesoscale regime when both *N*- and *U*-scattering coexist.[11–13] At the same time, novel materials (such as diamond, high-quality silicon,[14,15] graphene,[17–19,29–31] graphite, carbon nanotubes,[32–34] single-chain polymers,[35–44] superlattices,[22,45–47] and amorphous metals)[48,49] exhibit large phonon MFPs extending from micrometers to millimeters.[7,17–19,50–53] Consequently, even macroscale samples of these materials operate in the ballistic–diffusive regime, where interface scattering and nonlocal effects strongly influence heat flow and can dominate the effective thermal conductivity.[54–58] This results in sample length dependent heat fluxes[59] and thermal conductivities.[19,29–31,60–62]

In these circumstances, the thermal properties inferred from diffusive-limit concepts become misleading.[62–68] In reality, the heat conduction depends on resistive scattering lengths, the strength of normal scattering, sample geometry, and boundary conditions. Discrepancies among analytical models become most pronounced in cases when (i) the thermal Kn is large, (ii) temperature gradients are sharp,[65–68] (iii) heating/excitation timescales approach phonon relaxation times, and (iv) the heat flux approaches the *Casimir* limit due to a significant ballistic contribution.[5,9]

To address heat transport in this intermediate regime, a range of numerical approaches have been developed, including first-principles *Boltzmann* transport calculations coupled with density functional theory,[10,51,69,70] molecular dynamics simulations,[71–73] *Monte Carlo* solvers of the phonon *Boltzmann* equation,[73–77] and finite-volume formulations of phonon radiative transport.[5,78] A computationally efficient alternative is the Lattice–*Boltzmann–Peierls–Callaway* (LBPC) method, which discretizes the *Boltzmann–Peierls–Callaway* equation [79] and incorporates normal and Umklapp scattering through separate relaxation channels.[52,80–87] LBPC has been successfully applied to second sound, mesoscale size effects, hydrodynamic phonon flow, *Kapitza* resistance, and phonon MFP spectrum reconstruction[80–92] while maintaining the computational efficiency characteristic of lattice *Boltzmann* solvers.[88–92]

Despite these advances, a fundamental difficulty remains: outside the diffusive regime, there is no widely accepted definition of an effective phonon MFP or a corresponding bulk thermal conductivity that remains valid across different geometries and boundary conditions. When the sample length approaches or falls below the resistive scattering length, effective transport properties become controlled by a combination of intrinsic phonon scattering, boundary interactions, and the relative contributions of ballistic and diffusive heat flow.[12,21,28,65–67,93] This ambiguity complicates modeling and interpretation in applications ranging from ultrafast laser heating[94–99] and thermoelectric energy conversion[61,100–103] to nanoelectronics thermal management,[16,104–107] thermophones,[108–115] and nanoscale information storage.[116,117]

The *McKelvey–Shockley* Flux Method (MSFM)[118–122] provides a compact flux-based framework for phonon transport by expressing heat flow in terms of forward- and backward-propagating energy carriers.[5,6,65–67,121,122] In its general form, the MSFM applies to both transient and steady-state conditions; however, the formulation considered here is restricted to steady-state transport. The MSFM naturally yields directional heat fluxes and boundary temperature-jump conditions, but it does not, by itself, provide a closed analytical expression for the effective backscattering length and the related effective thermal conductivity in the ballistic–diffusive regime or specify how transmitted (ballistic) and backscattered (diffusive) phonon fluxes combine.[11–13]

In this work, the MSFM is extended to derive an analytical decomposition of the total heat flux and to establish a mesoscale thermal law (effective thermal conductivity) that extends the dependency beyond the Knudsen number to an effective backscattering length, and a bulk-like thermal conductivity. These quantities can be shown to arise naturally within the MSFM formulation but cannot be determined from it alone. To identify them, we perform systematic steady-state "mathematical experiments" using a D3Q19 LBPC model.[80–86] By varying the sample thickness and ballistic–diffusive mixing parameter for a set of materials (each with its own phonon dispersion, i.e., heat capacity), the LBPC simulations generate temperature fields and heat fluxes over a range of mesoscale conditions. From the collapse of all simulations into a unified mapping, the effective thermal conductivity is derived, from which an effective phonon MFP and a bulk-like thermal conductivity are extracted and used to close the MSFM relations. The main contribution is an MSFM–LBPC closure workflow to provide an internally consistent mesoscale framework in which the MSFM provides the analytical structure of ballistic–diffusive transport, while LBPC supplies the transport parameters required to determine scattering lengths, internal transmission and reflection fractions, and boundary temperature jumps, thereby reducing the degrees of freedom in the model.

II. THEORY AND APPROACH

This section summarizes the analytical framework used to interpret mesoscale heat transport within the MSFM and the LBPC formulation of the Boltzmann transport equation (BTE). Full derivations and supporting expressions are provided in supplementary material A: MODELS. Here, we present the essential working equations, definitions, and modeling assumptions used in both the analytical MSFM predictions and the numerical LBPC simulations.

A. MSFM formulation

In the MSFM,[118–122] a constitutive relation is formulated for one-dimensional mesoscale heat transfer analysis;[65–67] further details are given in Eqs. (A2)–(A38) in the supplementary material. Within the MSFM two-flux closure, the local temperature parameterizes the local equilibrium distribution, which establishes a direct and transparent connection between the heat flux and the temperature and its gradient. A key feature of the MSFM

is that each boundary injects phonon flux into the material. The left boundary at $y = y_L$ injects a forward phonon flux,

$$F_L^+(y_L, \epsilon) = n_L^+(y_L, \epsilon)\frac{v_y^+}{2} = \frac{D(\epsilon)v_y^+}{2} f_{BE}(T_L, \epsilon), \tag{1}$$

and the right boundary at $y = y_R$ injects a backward phonon flux,

$$F_R^-(y_R, \epsilon) = n_R^-(y_R, \epsilon)\frac{v_y^+}{2} = \left[\frac{D(\epsilon)v_y^+}{2}\right] f_{BE}(T_R, \epsilon), \tag{2}$$

where T_L and T_R are the constant temperatures of the surroundings associated with the left and right boundaries, respectively. The factor 1/2 accounts for the probability of propagation in either the positive or negative direction. v_y^+ is the rms phonon speed along the y direction at the reference temperature T_0. The term $n(T, \epsilon) = D(\epsilon) f_{BE}(T, \epsilon)$ is total phonon between ϵ and $\epsilon + d\epsilon$, where $\epsilon = h\nu_g \mathrm{k}/2\pi$ is the phonon energy, $D(\epsilon) = 12\pi\epsilon^2/h^3 v_g^3$ is the density of states (DOS) of phonon, $f_{BE}(T, \epsilon) = 1/[e^{\epsilon/k_B T} - 1]$ is the Bose–Einstein distribution (equilibrium) at temperature T, h is Planck's constant, v_g is the phonon speed (magnitude of group velocity), k is the magnitude of the phonon wave vector, and k_B is the Boltzmann constant. Inside the material, the forward and backward phonon fluxes

$$F^{\pm}(y, \epsilon) = \left[\frac{D(\epsilon)\, v_y^+}{2}\right] f_{BE}(T^{\pm}, \epsilon) \tag{3}$$

propagate and undergo backscattering.

The corresponding directional heat fluxes $q^{\pm}(y, T^{\pm})$ are obtained by multiplying the phonon fluxes with the phonon energy and integrating over the entire phonon momentum space,

$$q^{\pm}(y, T^{\pm}) = \int_0^{\infty} \epsilon F^{\pm}(y, \epsilon) d\epsilon = \frac{v_y^+}{2}\frac{4\sigma_{SB}}{v_g}(T^{\pm})^4, \tag{4}$$

where $\sigma_{SB} = \pi^5 k_B^4/(5h^3 v_g^2)$ is the *Stefan–Boltzmann* constant. The forward and backward heat fluxes $q^+(y, t)$ and $q^-(y, t)$ evolve according to[66]

$$\frac{1}{v_y^+}\frac{\partial q^+}{\partial t} + \frac{\partial q^+}{\partial y} = -\frac{q^+}{\Lambda_b} + \frac{q^-}{\Lambda_b} \text{ and } \frac{1}{v_y^+}\frac{\partial q^-}{\partial t} + \frac{\partial q^-}{\partial y} = -\frac{q^+}{\Lambda_b} + \frac{q^-}{\Lambda_b}. \tag{5}$$

Here, $\Lambda_b = \tau_b v_y^+$ is the backscattering length, where the backscattering time τ_b is treated as independent of temperature and the frequency of external excitation, as assumed in the gray approximation.[121]

It is important to note that Eq. (5) may be applied to each boundary temperature independently. For example, if $T_R = T_0$, then the left boundary temperature T_L generates both forward and backward flux components, with $q^+ > q^-$, leading to a positive net heat flux $q = q^+ - q^-$. Conversely, if $T_L = T_0$, then the right boundary temperature T_R induces $q^+ < q^-$, producing a negative net heat flux. Thus, each boundary temperature generates both directional components, and the net heat flux is always $q = q^+ - q^-$. In contrast, the total phonon density is direction independent and governed only by the local temperature, which can be obtained as the average of the directional temperatures, $T = (T^+ + T^-)/2$. Therefore, when two or more boundary temperatures are prescribed, a consistent relation must be established between the directional fluxes $q^{\pm}$ and the directional temperatures $T^{\pm}$, which represent both the phonon density and the directional phonon populations.

However, Eq. (5) alone does not yield $q^{\pm}$ directly from the specified temperatures T_L, T_R, and T_0, because heat fluxes and temperatures are related through the ballistic thermal conductance G_0. Specifically, $q^{\pm} = G_0 T^{\pm}$, $\delta q^{\pm} = G_0\, \delta T^{\pm}$, where G_0 is the ballistic thermal conductance per unit area, corresponding to a ballistic thermal resistance $R_0 = 1/(AG_0)$. The associated ballistic conductivity is $k_0 = G_0 L_y$. Since G_0 is a quantum limit of phonon heat transport, it is independent of the sample length. Accordingly, in the ballistic regime, effective thermal conductivity satisfies $k_{\text{eff}} \to k_0 \propto L_y$. In the opposite limit, when bulk scattering dominates, k_{eff} approaches the asymptotic diffusive conductivity k_∞, which is independent of system size. Thus, the heat-transport regime transitions smoothly from ballistic to diffusive as the mixing parameters of Umklapp (λ_U) and normal (λ_N) processes, the Umklapp MFP Λ_U, and the domain thickness L_y vary. These scattering mixing parameters, λ_U and λ_N, are re-introduced and defined later in the LBPC formulation.

Nevertheless, Eq. (5) can be solved numerically by using boundary injected heat fluxes (q_L^+ and q_R^- at temperatures T_L and T_R, respectively) and reference heat flux of q_{eq}. The conversion from q to T is done by using

$$\begin{aligned} q^{\pm} &= G_0 T^{\pm};\ q^+(y = y_L) = q_L^+ = G_0 T_L, \\ q^-(y = y_R) &= q_R^- = G_0 T_R \text{ and} \\ q^{\pm}(y, T_0) &= q_{eq}(y, T_0) = \sigma_{SB} T_0^4 = G_0 T_0, \end{aligned} \tag{6}$$

where $G_0 = (v_y^+/2)16\sigma_{SB} T_0^3/v_g$. Similar expressions can be obtained for the forward/backward deviatoric heat fluxes $\delta q^{\pm} = q^{\pm} - q_0$ and temperatures $\delta T^{\pm} = T^{\pm} - T_0$ with a conversion factor $\delta T^{\pm} = \delta q^{\pm}/G_0$. Knowing solutions of $T^{\pm}$, the net/total heat flux is obtained by $q = q^+ - q^- = G_0(T^+ - T^-)$ and the local energy density can be found through $e = (q^+ + q^-)/v_y^+ = C_V(T^+ + T^-)/2 = C_V T$, with $G_0 = C_V v_y^+/2$ and $C_V = de/dT = 16\sigma_{SB} T_0^3/v_g$ being the specific heat capacity of the material. Note that all subsequent equations, in this MSFM, could use terms either the standard form $(T^{\pm}, T_0, T_{L/R})$ or deviatoric form $(\delta T^{\pm}, \delta T_0, \delta T_{L/R})$. If terms $(\delta T^{\pm}, \delta T_0, \delta T_{L/R})$ are used in the subsequent equations, the expression of net heat flux $q = \delta q^+ - \delta q^- = G_0(\delta T^+ - \delta T^-) = G_0(T^+ - T^-)$ remains unaffected; however, local energy density has a deviatoric part $\delta e = (\delta q^+ + \delta q^-)/v_y^+ = C_V(\delta T^+ + \delta T^-)/2 = C_V \delta T$ from the equilibrium energy density $e_{eq} = C_V T_0$ with $C_V = d\delta e/d\delta T = 16\sigma_{SB} T_0^3/v_g$.

The fluxes q^+ and q^- can be expressed in terms of e and q as follows:

$$2q^+ = v_y^+ e + q \text{ and } 2q^- = v_y^+ e - q. \tag{7}$$

The above equation will be used to determine BCs for T or $T^\pm$ because of the known temperatures T_L and T_R applied on the left and right walls, respectively. Subtraction and addition of terms in Eq. (5) yields energy balance,

$$\frac{\partial e}{\partial t} + \frac{\partial q}{\partial y} = 0, \tag{8}$$

and the flux law

$$\frac{\Lambda_b}{2v_y^+}\frac{\partial q}{\partial t} + q = -\frac{C_V \Lambda_b v_y^+}{2}\frac{\partial T}{\partial y} \tag{9}$$

for heat transfer in the MSFM. Here, $C_V \Lambda_b v_y^+/2 = k_\infty$ is thermal conductivity (traditionally $k_\infty \cong C_V \Lambda_U v_g/3$)[5,65] of the material, $\Lambda_b v_y^+/2 = D_{ph}$ is the phonon diffusivity (traditionally $D_{ph} \cong \Lambda_U v_g/3$), $\Lambda_b/2v_y^+ = \tau_Q$ is thermal relaxation time (traditionally $\tau_Q \cong 4\tau_U/3$), and $v_y^+ = \sqrt{D_{ph}/\tau_Q} = v_g/2$ is the thermal speed (traditionally $v_y^+ = v_g/\sqrt{3}$ for CV, DPL, and GK).[5,26] $v_y^+ = v_g/2$ gives the actual value of $G_0 = C_V v_g/4$, and the traditional value of $\Lambda_b \cong 4\Lambda_U/3$[5,122] produces $k_\infty = G_0 \Lambda_b = C_V \Lambda_U v_g/3$.[5,65] Note that Eq. (9) relates the driving force $q^+ - q^-$ for drift with the driving force $-k_\infty(\partial T/\partial y)$ for diffusion.

At steady state, the equations can be reduced to the following expressions:

$$\frac{dq}{dy} = 0 \text{ and } q = -k_\infty \frac{dT}{dy}, \tag{10}$$

which gives us $q \neq q(y)$, yielding the following:

$$\frac{dq^+(y)}{dy} = \frac{dq^-(y)}{dy} = -\frac{q}{\Lambda_b} \text{ and } \frac{d^2T(y)}{dy^2} = 0. \tag{11}$$

As $q \neq q(y)$ at the steady state, Eq. (10) is used to find the drift heat flux $q = q^+ - q^-$ via

$$q = G_0(T^+ - T^-) = -G_0 \Gamma \Delta T_b, \tag{12}$$

where $\Delta T_b = T_R - T_L$ and $\Gamma = \Lambda_b/[\Lambda_b + L_y]$ is the internal transmission fraction. Note that the heat flux q is quite different from the heat flux $-k_\infty(\partial T/\partial y)$ due to the fact that q vanishes as $\Gamma \to 0$ (diffusive limit, $L_y \gg \Lambda_b$); however, $\partial T/\partial y$ does not. The temperature distribution T is given as

$$T(y) = T(y_L) + \mathrm{R}\frac{(y - y_L)\Delta T_b}{L_y} = T_m + \frac{(y - y_m)\Delta T_b}{L_y + \Lambda_b}, \tag{13}$$

where $\mathrm{R} = 1 - \Gamma = L_y/[L_y + \Lambda_b]$ is the internal reflection fraction, $T_m = (T_L + T_R)/2$, and $y_m = (y_L + y_R)/2$. The solution, in Eq. (13), is obtained upon use of $d^2T(y)/dy^2 = 0$ subjected to the jump boundary temperatures.

$$T(y_L) = T_P = \frac{T^+(y_L) + T^-(y_L)}{2} = (2 - \Gamma)\frac{T_L}{2} + \Gamma\frac{T_R}{2} = T_L + \Gamma\frac{\Delta T_b}{2} \text{ and}$$
$$T(y_R) = T_M = \frac{T^+(y_R) + T^-(y_R)}{2} = \Gamma\frac{T_L}{2} + (2 - \Gamma)\frac{T_R}{2} = T_R - \Gamma\frac{\Delta T_b}{2}, \tag{14}$$

which are being derived from steady-state solutions of $q^\pm$ at boundaries. One can solve $d^2T(y)/dy^2 = 0$ from Eq. (10) to get the same solution of $T(y)$, as given in Eq. (13), by using the jump BCs as follows:

$$-\frac{\Lambda_b}{2}\left(\frac{dT}{dy}\right)_{y=y_L} + T(y_L) = T_L \text{ and } \frac{\Lambda_b}{2}\left(\frac{dT}{dy}\right)_{y=y_R} + T(y_R) = T_R, \tag{15}$$

without exact expressions of $T(y_L)$ and $T(y_R)$, in contrast to Eq. (14). The jump BCs, in Eq. (15), are derived from expressions given in Eq. (7) after the substitution of $e = C_V T$ to form $q = -(C_V \Lambda_b v_y^+/2)(dT/dy)$ with relations $2q_L^+ = C_V v_y^+ T_L$ and $2q_R^- = C_V v_y^+ T_R$. Note that Eq. (15) provides the jump BC form required to embed mesoscale effects into continuum solvers (Fourier and the transient CV/DPL frameworks). At steady state, CV/DPL reduce to Fourier as $\partial/\partial t$ vanishes and reduces to Eq. (10), making these formulations analogous to one another and to Fourier model with energy conservation. The corresponding temperature gradient (dT/dy) and diffusion heat flux $q = -k_\infty(dT/dy)$ can be calculated from the following expressions:

$$\frac{dT}{dy} = -\mathrm{R}\frac{\Delta T_b}{L_y} \text{ and } q = -k_\infty \mathrm{R}\frac{\Delta T_b}{L_y}. \tag{16}$$

Both the temperature gradient and diffusion heat flux vanish as $\mathrm{R} \to 0$ (ballistic limit, $L_y \ll \Lambda_b$); however, the drift heat flux $q = G_0(T^+ - T^-) = -G_0 \Gamma \Delta T_b$ does not.

The quantities appearing in Eqs. (12)–(16) depend on two internal fractions, transmission Γ, and reflection R, which must be defined for carriers within the material (such as for phonons in crystalline solids). Then, the MSFM flux law can be written in a form that separates gradient-driven and backscattering-related contributions; this is a decomposition of the same net flux, not two independent transport channels. Based on these observations and the analysis in Refs. 65–67, the present work extends the description of the total heat flux q, receiving contributions from diffusive and ballistic transport,

$$q_d = -k_\infty \mathrm{R}\frac{\Delta T_b}{L_y}\ ;\ q_b = q - q_d = -k_0 \Gamma \frac{\Delta T_b}{L_y} \Rightarrow q = q_b + q_d = -(k_\infty \mathrm{R} + k_0 \Gamma)\frac{\Delta T_b}{L_y}. \tag{17}$$

The total heat flux q can be normalized based on the maximum heat flux (q_m) available in the system for pure ballistic transport $(\Gamma = 1)$ analogous to the radiation heat transfer case and calculated

from the Casimir limit[5] as

$$q_{\mathrm{m}} = q_L^{+} - q_R^{-} = \sigma_{SB}\left(T_L^4 - T_R^4\right) = -G_0 \Delta T_b. \tag{18}$$

The effective thermal conductivity (k_{eff}) can be obtained, by using the quasi-static relation,

$$q = -k_{\mathrm{eff}} \frac{\Delta T_b}{L_y}, \tag{19}$$

and comparison with Eq. (17) gives

$$k_{\mathrm{eff}} = k_\infty \mathrm{R} + k_0 \Gamma = \frac{k_\infty L_y + k_0 \Lambda_b}{\Lambda_b + L_y} = \frac{k_{\mathrm{bulk}} L_y}{\Lambda_b + L_y}, \tag{20}$$

where $k_{\mathrm{bulk}} = k_\infty + G_0 \Lambda_b$ is the bulk-like thermal conductivity in diffusive–ballistic heat transport. Equation (20) recovers both the diffusive ($L_y \gg \Lambda_b$) and the ballistic ($L_y \ll \Lambda_b$) limits. Note that Eq. (20) provides a compact closed form for the thickness dependent effective conductivity that recovers the expected asymptotes: in the diffusive limit $k_{\mathrm{eff}} \to k_{\mathrm{bulk}}$ and in the ballistic limit $k_{\mathrm{eff}} \to G_0 L_y$. This expression is most naturally interpreted as a finite-size backscattering (jump/attenuation) correction to a bulk-like conductivity (which can serve as a new reference for material characterization), and it should not be interpreted as the parallel addition of independent heat transfer channels. Rearranging Eq. (20), one can obtain

$$\frac{1}{k_{\mathrm{eff}}} = \frac{1}{k_{\mathrm{bulk}}} + \frac{\Lambda_b}{k_{\mathrm{bulk}}} \frac{1}{L_y}. \tag{21}$$

Note that two distinct quantities k_∞ and $G_0 \Lambda_b$ coexist in ballistic–diffusive mesoscale heat transfer models, unlike the classical representations resulting in $k_\infty = G_0 \Lambda_b = C_V \Lambda_U v_{\mathrm{g}}/3$.[65] It is also important to point out that the vastly used $\Lambda_b = 4\Lambda_U/3$[5,122] value is not valid for the diffusive-ballistic crossover. Therefore, the current MSFM formulation presents the need for re-evaluating the validity of some relationships in mesoscale heat transfer, such as C_V, $G_0 = C_V v_{\mathrm{g}}/4$, Λ_b (as $\Lambda_b \neq 4\Lambda_U/3$ in general), k_∞ (as $k_\infty \neq G_0 \Lambda_b = C_V \Lambda_U v_{\mathrm{g}}/3$ in general), $k_0 = G_0 L_y$, and $k_{\mathrm{bulk}} = k_\infty + G_0 \Lambda_b$. Therefore, the present work uses the LBP framework to formulate relationships empirically for these parameters.

B. LBPC formulation

In the present work, the LBPC solution method is based on the approach introduced in Refs. 79–84. The BPC equation

$$\left(\frac{\partial}{\partial t} + \mathbf{v}_{\mathrm{g},\mathbf{k}}^{\sigma} \cdot \nabla_{\boldsymbol{r}}\right) f^{\sigma}(t, \boldsymbol{r}, \mathbf{k}) = \frac{f_N^{\sigma,\mathrm{eq}} - f^{\sigma}}{\tau_N} + \frac{f_U^{\sigma,\mathrm{eq}} - f^{\sigma}}{\tau_U} \tag{22}$$

describes the polarized single phonon nonequilibrium distribution $f^{\sigma}(t, \boldsymbol{r}, \mathbf{k})$. The relaxation time τ_U represents scattering processes that conserve energy but degrade crystal momentum—Umklapp events, boundary scattering, and impurity scattering (U-processes). Conversely, τ_N represents the normal three-phonon interactions conserving both energy and momentum (N-processes). Both relaxation times and the group velocity depend on phonon branch, polarization, dispersion relation, and temperature.

The corresponding discrete (D3Q19) LBPC formulation is

$$\begin{aligned} f_i^{\sigma}\left(\boldsymbol{r} + \boldsymbol{c}_i \Delta t, t + \frac{c}{v_{\mathrm{g}}^{\sigma}} \Delta t\right) &= f_i^{*\sigma}(\boldsymbol{r}, t) \\ &= (1 - \lambda_N - \lambda_U) f_i^{\sigma} + \lambda_N f_{i,N}^{\sigma,eq} \\ &\quad + \lambda_U f_{i,U}^{\sigma,eq}, \end{aligned} \tag{23}$$

where f_i^{σ} is updated every $c/v_{\mathrm{g}}^{\sigma} = c(1+\sigma)/v_{\mathrm{g}} = (1+\sigma)$ time steps choosing $c = v_{\mathrm{g}}$. Equation (23) addresses the directional polarized single phonon nonequilibrium distribution f_i^{σ} with mixing parameters $\lambda_{N[U]} = c\Delta t/\tau_{N[U]} v_{\mathrm{g}}^{\sigma} = \Delta x/\Lambda_{N[U]}$. Here, c is the unit speed (representing the speed of sound) and Δx is the lattice spacing in the lattice *Boltzmann* method (LBM) (corresponding physically to a characteristic crystal spacing). Then, Δt is the average time required for a phonon to travel between lattice sites. v_{g}^{σ} is the polarized group velocity of phonons, defined as $v_{\mathrm{g}}^{\sigma} = v_{\mathrm{g}}/(1+\sigma)$, where v_{g} is the intrinsic group velocity or speed of sound in the medium and σ represents the polarization of phonons (0 for longitudinal acoustic and 1 for transverse acoustic). This formulation consists of two independent steps in LBM: (i) collision

$$f_i^{*\sigma} = (1 - \lambda_N - \lambda_U) f_i^{\sigma} + \lambda_N f_{i,N}^{\sigma,eq} + \lambda_U f_{i,U}^{\sigma,eq} \tag{24}$$

and (ii) streaming

$$f_i^{\sigma}\left(\boldsymbol{r} + \boldsymbol{c}_i \Delta t, t + \frac{c}{v_{\mathrm{g}}^{\sigma}} \Delta t\right) = f_i^{*\sigma}(\boldsymbol{r}, t), \tag{25}$$

respectively. The spatial resolution of the LBM, Δx, is constrained to be less than or equal to the phonon MFP $\Lambda_{N,U}$, i.e., $\Delta x \leq \Lambda_{N[U]} = v_{\mathrm{g}}^{\sigma} \tau_{N[U]}$, thus limiting $\lambda_{N[U]} \leq 1$. To avoid the overdamping of f_i^{σ}, the value of the parameter $1 - \lambda_N - \lambda_U \geq 0$ must be maintained and kept close to zero to prevent anisotropic heat wave propagation from lattice point sources and to ensure coarser spatiotemporal resolution of temperature.[83] As $c = v_{\mathrm{g}}$ (LBM speed is equal to the magnitude of the intrinsic phonon group velocity in the region), a newly defined combined mixing parameter can be defined as $\lambda_c = \Delta x/\Lambda_c = c\Delta t/v_{\mathrm{g}}^{\sigma}\tau_c = \lambda_N + \lambda_U$. We choose the spatial discretization of LBM as $\Delta x = c\Delta t = \Lambda_c$, so we have the temporal discretization $\Delta t = v_{\mathrm{g}}^{\sigma}\tau_c/c$, which also makes the relation $1 - \lambda_N - \lambda_U = 0$ true. Therefore, one must choose λ_U (indicates the diffusion transport by means of U-processes at the lattice level) and calculate $\lambda_N = 1 - \lambda_U$ (indicates the ballistic transport by means of N-processes) for LBPC simulations.

After streaming, the local equilibrium distribution is approximated linearly from the global equilibrium distribution function, subjected to local disturbances of macroscopic collision invariants as assumed in LBM. Global thermal equilibrium is established at all lattice sites with an initial temperature T_0 and drift velocity $\mathbf{u}_0 = 0$, resulting in the phonon *Planck* distribution function [as given in Eq. (A47) in the supplementary material]. The local equilibrium distribution at $(\boldsymbol{r}, t)$ can be approximated to the first order

of the global equilibrium perturbation [as given in Eqs. (A48) and (A49) in the supplementary material for the weighted *Planck* distribution $f_{i,U}^{\sigma,eq}$ and the weighted displaced *Planck* distribution $f_{i,N}^{\sigma,eq}$, respectively], subjected to temperature perturbations $\theta = (T - T_0)/T_0$ and the phonon drift velocity $\tilde{\mathbf{u}} = (\mathbf{u} - \mathbf{u}_0)/v_g$ from T_0 and $\mathbf{u}_0$. The Taylor series expansions of equilibrium distributions are provided in Eqs. (A50) and (A51) in the supplementary material about $\theta = 0$ and $\tilde{\mathbf{u}} = 0$.

Once f_i^σ is determined, the macroscopic quantities such as energy density E (in dimensions of $[n_p k_B T_0]$, J/m^3), momentum density $\boldsymbol{P}$ (in dimensions of $[n_p k_B T_0/v_g]$, N s/m^3), and heat flux $\boldsymbol{Q}$ (in dimensions of $[v_g n_p k_B T_0]$, W/m^2) are computed using

$$E(\boldsymbol{r}, t) = \sum_{\sigma,i} \epsilon_i^\sigma f_i^\sigma(\boldsymbol{r}, t),\ \boldsymbol{P}(\boldsymbol{r}, t) = \sum_{\sigma,i} \mathbf{p}_i^\sigma f_i^\sigma(\boldsymbol{r}, t) \text{ and } \boldsymbol{Q}(\boldsymbol{r}, \boldsymbol{t}) = \boldsymbol{Q}^{\text{pre}}(\boldsymbol{r}, \boldsymbol{t}) + \boldsymbol{Q}^*(\boldsymbol{r}, \boldsymbol{t}), \tag{26}$$

where $\mathbf{Q}^{\text{pre}} = \sum_{\sigma,i} \mathbf{v}_{gi}^\sigma \epsilon_i^\sigma f_i^\sigma = v_g^2 \mathbf{P}^{\text{pre}}$ is the pre-collision heat flux and $\mathbf{Q}^* = \sum_{\sigma,i} \mathbf{v}_{gi}^\sigma \epsilon_i^\sigma f_i^{*,\sigma} = v_g^2 \mathbf{P}^*$ is the post-collision heat flux. The calculations for θ and $\tilde{\mathbf{u}}$ must precede the collision step to determine $f_{i,U}^{\sigma,eq}$ and $f_{i,N}^{\sigma,eq}$, for which the conservation laws for the local collision invariants are applied,

$$\theta(\boldsymbol{r}, t) = \frac{E(\boldsymbol{r}, t) - M_1}{M_2} \text{ and } \tilde{\mathbf{u}}(\boldsymbol{r}, t) = \frac{\mathbf{P}(\boldsymbol{r}, t) - \boldsymbol{V}(\boldsymbol{r}, t)}{M_3}, \tag{27}$$

where $M_1 = \sum_{\sigma,i} \epsilon_i^\sigma \omega_i^\sigma A_i^\sigma$, $M_2 = -\beta_0 \sum_{\sigma,i} (\epsilon_i^\sigma)^2 \omega_i^\sigma B_i^\sigma$, $\boldsymbol{V} = \sum_{\sigma,i} \mathbf{p}_i^\sigma \omega_i^\sigma (A_i^\sigma - \beta_0 \epsilon_i^\sigma B_i^\sigma \theta) \sum_{\sigma,i} \mathbf{p}_i^\sigma f_{i,U}^{\sigma,eq}$ and $M_3 = -\beta_0 \epsilon \sum_{\sigma,i} \omega_i^\sigma B_i^\sigma \mathbf{p}_i^\sigma \cdot \boldsymbol{e}_i$.

C. Domain and BCs

Using this LBPC formulation, a series of mathematical experiments are designed to determine the effective thermal conductivity over a range of mixing parameters and sample thicknesses. This strategy enables a controlled transition from the macroscale (diffusive) to the mesoscale (ballistic–diffusive) regime by varying only the scattering parameters and the domain thickness—without modifying the underlying LBM code.

We consider an insulator or semiconductor solid, as shown in Fig. 1, bounded by $x_L \le x \le x_R$, $y_L \le y \le y_R$, and $z_L \le z \le z_R$, and where the lateral dimensions in the x and z directions are assumed to be much larger than the length in the y direction,

$$L_x = x_R - x_L,\ L_z = z_R - z_L,\ L_y = y_R - y_L, \text{ and } L_y \ll (L_x, L_z).$$

Therefore, we kept $L_x = 3\Delta x$ and $L_z = 3\Delta z$ for all simulations while applying periodic BCs in these directions (see Fig. 1) so that heat transfer is effectively one-dimensional and confined to the y direction, free from lateral wall effects. To match LBPC results with the real physics, the boundaries are treated by a jump condition, upon considering only Umklapp phonon scattering locally with constant temperatures T_L and T_R, respectively.[83] Therefore, we do not need to specify any additional BCs in the y direction.

As the mixing parameters are defined by $\lambda_{N[U]} = \Lambda_c/\Lambda_{N[U]}$, $\Lambda_c^{-1} = \Lambda_N^{-1} + \Lambda_U^{-1}$ with $\Delta x = \Delta y = \Delta z = \Lambda_c$ imposed by the LBM selection, LBPC simulations encode the combined relaxation time $\tau_c^{-1} = \tau_N^{-1} + \tau_U^{-1}$, $\Lambda_c = \tau_c v_g$, $\Delta t = \tau_c$ by selecting appropriate τ_U and τ_N, while the LBM streaming speed has been set to $c = v_g$.

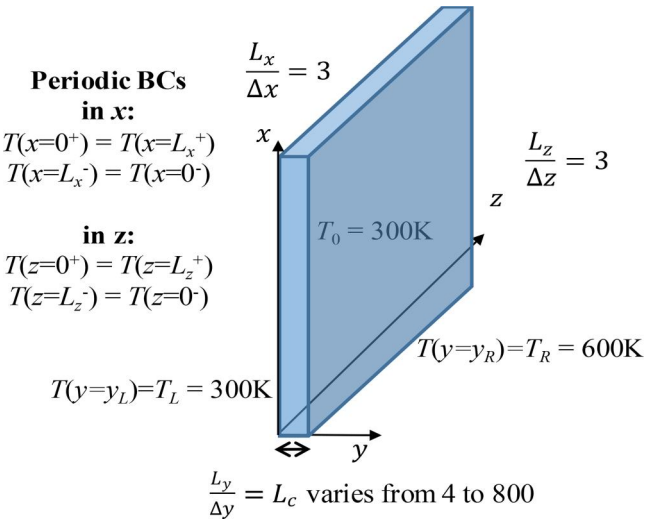

FIG. 1. Schematic of the numerical LBPC domain with boundary and initial conditions.

Given the mixing parameter λ_U, the MFP of the U-process ($\Lambda_U = \tau_U v_g$) and the thermal *Knudsen* number ($\text{Kn} = \Lambda_U/L_y = 1/\lambda_U L_c$) are then known. In LBPC formulation, the value of λ_U controls the relative contribution of heat transfer mechanism and therefore shifts the solution from the diffusive to the ballistic limit. In the present LBPC parameterization, the control knob is $1/\lambda_U$ (equivalently Kn as defined here). The U-dominated diffusive limit corresponds to $\lambda_U \to 1$ (i.e., $1/\lambda_U \to 1$, $\lambda_N \to 0$), for which the effective attenuation length becomes negligible, and the conductivity is thickness independent. The ballistic limit corresponds to $\lambda_U \to 0$ (i.e., $1/\lambda_U \to \infty$, $\lambda_N \to 1$), for which the effective attenuation length approaches the U-process scattering length and the effective conductivity scales linearly with thickness. When $0 \le \lambda_U \le \lambda_N \le 1$, it is a ballistic–diffusive process as it gives $0 < \Delta y = \Lambda_c < \Lambda_N < \Lambda_U$, $0 < \Delta t = \tau_c < \tau_N < \tau_U$, and $0 < L_y/\Lambda_U = 1/Kn < \infty$.

D. Assumptions

The MSFM formulation assumes 1D transport along the longitudinal y direction (with no gradients along the two other directions), forming a thin film domain consistent with the two-flux description. In the current formulation, the problem is treated as the steady state in the closed form of $k_{\text{eff}}(L_y)$ and with a jump BC. The backscattering is represented as a single characteristic length according to gray approximation (Λ_b, analogous to Λ_{eff} later), rather than a full spectral collision operator; and accordingly, single effective speed (rms speed/group velocity) is utilized at a reference temperature. A degeneracy factor is used to represent the branch/polarization resolution. Jump conditions are used to embed mesoscale effects into the continuum form of the jump BCs.

Then, in order to provide the closure parameters (backscattering length/effective MFP and bulk-like conductivity) to the MSFM, the LBPC is used under the following assumptions. For a given mixing parameter combination, the dispersion/heat capacity is kept constant for all sample thicknesses, which implies that the dependence on length scale arises from finite-size/backscattering effects. Moreover, at the boundaries, momentum-destroying scattering is only represented through the adopted U-processes.

E. Design of experiments

In the mathematical experiment, the initial (reference) temperature is assumed uniform, $T_0 = 300$ K, throughout the domain. A temperature rise is imposed at the right boundary $y = y_R$ such that $T_R = 600K > T_0$, while the left boundary at $y = y_L$ is held at $T_L = T_0$, Fig. 1. The material type is selected by taking one of the four combinations of longitudinal acoustic and optical phonon energies, ϵ_A^0 and ϵ_O^0, given in Table I. The phonon energy parameters, acoustic ϵ_A^σ and optical ϵ_O^σ, are expressed nondimensionally as multiples of $k_B T_0 = 25.8$ meV. These energies define the material's dispersion characteristics (see Refs. 1–4 and 65 for information on phonon dispersion relations) and establish a direct correlation to the specific heat capacity of the material. A fixed value of the mixing parameter λ_U is used to introduce ballistic diffusive nature for a sample thickness $L_y = L_c \Delta y$. A set of 16 values of λ_U: 1.0, 0.5, 0.25, 0.20, 0.125, 0.1, 0.0625, 0.05, 0.04, 0.02, 0.01, 0.008, 0.004, 0.002, 0.00125, 0 are tested for each of the 14 values of L_c: 4, 5, 6, 7, 8, 10, 16, 20, 25, 50, 100, 200, 500, 800. Each combination of λ_U, L_c, and energy pair $(\epsilon_A^0, \epsilon_O^0)$ free variables provides a simulation point in the multidimensional mathematical experiment grid $(16 \times 14 \times 4 = 896)$. Then, the steady-state temperature and heat flux fields are obtained, facilitating to determine the effective conductivity and subsequently used to extract the phonon MFP and bulk-like thermal conductivity.

F. Parameter estimation

Identification of the MSFM parameters in LBPC formulation starts with ballistic thermal transport when $\lambda_U = 0$, for which the maximum steady-state heat flux $Q_{y,m}$ is given in Eq. (18) (*Casimir* limit[5]) and the ballistic thermal conductance per unit area, G_{ball} [in dimension of $(v_g n_p k_B)$ W/m^2 K], is calculated using

$$G_0 = \frac{|\vec{q}(\boldsymbol{r}, t)|_{\max}}{\Delta T_b} = Q_{y,m} \times \frac{v_g n_p k_B T_0}{\theta_b T_0} = G_{\text{ball}} \times v_g n_p k_B \Rightarrow G_{\text{ball}} = \frac{Q_{y,m}}{\theta_b}. \tag{28}$$

TABLE I. Description of test sample material type with phonon energy/dispersion relations.

	$\epsilon_A^0 (k_B T_0)$	$\epsilon_O^0 (k_B T_0)$
Sample 1	0.535 95	1.0
Sample 2	0.935 95	1.0
Sample 3	1.535 95	2.0
Sample 4	1.927	2.0

Note that all our calculations consider $\theta_b = 1$, which yields $G_{\text{ball}} = Q_{y,m}$.

The classical or quasi-static relationship between heat flux $(\vec{q})$ and temperature gradient (∇T) is used to calculate the dimensionless conductivity k [in units of $(v_g \Delta y n_p k_B)$, W/m K] from the following expression:

$$k_{\text{eff}} = |\vec{q}(\boldsymbol{r}, t)| \times \frac{L_y}{\Delta T_b} = Q_y \times \frac{v_g n_p k_B T_0 L_c \Delta y}{\theta_b T_0} = k \times v_g \Delta y n_p k_B \Rightarrow k = \frac{Q_y L_c}{\theta_b}. \tag{29}$$

Thus, once Q_y is known, the effective conductivity (k_{eff}) is obtained from $k = Q_y L_c / \theta_b$, based on the selected combination of free variables. The effective thermal conductivity k approaches its bulk-like value k_{LBPC} as the *Knudsen* number $\text{Kn} = 1/\lambda_U L_c$ tends to zero. In the LBPC framework, for a given τ_U, k increases proportionally with the sample thickness L_y and converges to k_{LBPC} as $L_y \to \infty$. Importantly, k_{LBPC} need not equal the diffusive-limit bulk conductivity k_{diff}, even when the transport appears predominantly diffusive.

For the LBPC framework, an effective conductivity expression analogous to Eq. (20) can be written for a given film thickness L_y,

$$k = \frac{k_{\text{LBPC}} L_y}{\Lambda_{\text{eff}} + L_y}, \tag{30}$$

where Λ_{eff} is the effective MFP. Rearranging Eq. (30) yields the following linear relation:

$$\frac{1}{k} = \frac{1}{k_{\text{LBPC}}} + \frac{\Lambda_{\text{eff}}}{k_{\text{LBPC}}} \frac{1}{L_y}. \tag{31}$$

Thus, for fixed τ_U, a series of conductivity measurements obtained by varying only L_y allow $1/k_{\text{LBPC}}$ and Λ_{eff} to be extracted from the intercept of the $1/k$ vs $1/L_y$ fit at $1/L_y \to 0$ and the slope-to-intercept ratio, respectively. When $L_y \gg \Lambda_{\text{eff}}$, the conductivity approaches the diffusive asymptote, $k = k_{\text{diff}} = k_{\text{LBPC}}$, and it is independent of sample thickness L_y. When $L_y \ll \Lambda_{\text{eff}}$, the conductivity is in the ballistic limit and grows linearly with thickness, $\Lambda_{\text{eff}} \to \Lambda_U$ and $k_{\text{LBPC}} \to G_{\text{ball}} \Lambda_U$, resulting in $k \to k_{\text{ball}} = G_{\text{ball}} L_y$, consistent with the absence of momentum-destroying U-processes. At finite L_y/Λ_{eff}, when the ballistic–diffusive transport processes both contribute.

G. Error estimation and convergence

The LBPC solver is a discrete-velocity LBM formulation for which drift is represented by exact streaming on the lattice and scattering is represented by relaxation toward prescribed equilibrium. The relevant numerical uncertainty is not the stochastic sampling error, but rather associated with discretization, boundary implementation, and parameter identification from finite-thickness data.

For sufficiently smooth fields and away from boundaries, the Chapman–Enskog consistency of LBM implies second-order accuracy in space and time for the recovered moments under diffusive

scaling, provided the chosen velocity set supplies the required isotropy of lower order moments. Consequently, in steady one-dimensional conduction, the leading truncation error in interior heat flux and temperature scales as $O(\Delta x^2)$ [and, with $\Delta t \propto \Delta x$, also $O(\Delta t^2)$], implying that discretization-driven deviations in Q_y and inferred k decrease approximately as $O(L_c^{-2})$. Therefore, the dominant discretization uncertainty is controlled by lattice resolution relative to the imposed gradients and boundary layer thickness (1/2 grid in the study).

In the present D3Q19 LBPC scheme, as the lattice spacing and time step are tied to the selected characteristic relaxation scales through $\Delta x = \Delta y = \Delta z = \Lambda_c$ and $\Delta t = \tau_c$ (with streaming speed $c = v_g$), Δx and Δt are part of the physical mapping of the model rather than freely tunable numerical parameters. Therefore, "grid refinement" can be interpreted as a controlled change in lattice resolution relative to the imposed scattering scales, and in this case, the value is set to 1, the lowest limit of the lattice size.

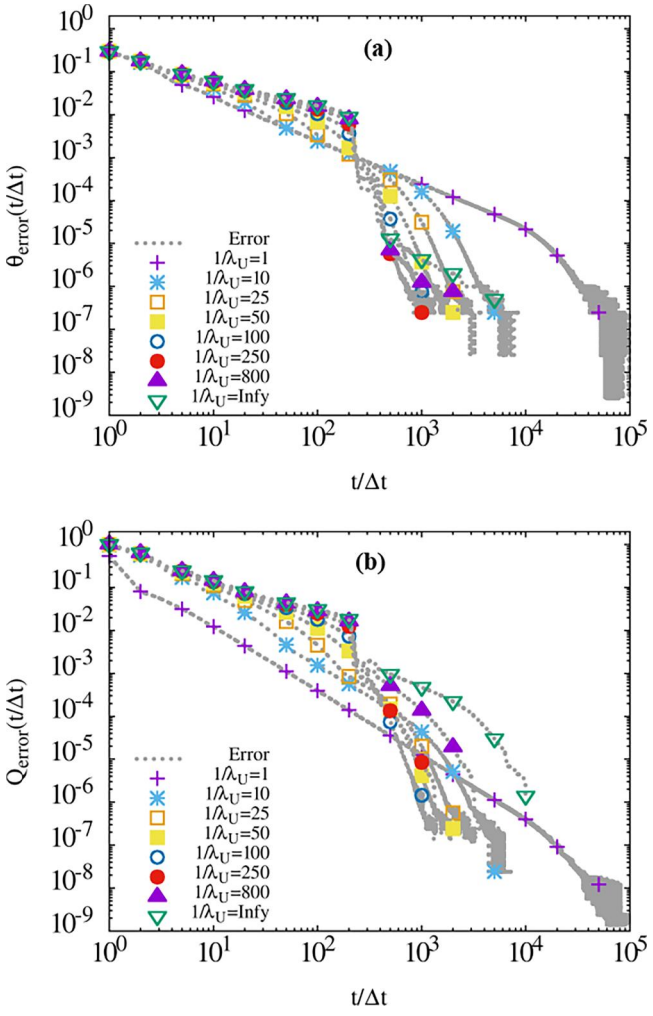

FIG. 2. Residuals of (a) temperature and (b) heat flux with time steps $t/\Delta t$ for sample size $L_y = 100\Delta y$, considering a range of mixing parameters.

TABLE II. Predictive holdout accuracy and extraction-window sensitivity for effective thermal conductivity and closure parameter estimations.

λ_U^{-1}	$\bar{\varepsilon}(10^{-6})$	$\frac{\Delta k_{LBPC}}{k_{LBPC}}(10^{-6})$	$\frac{\Delta\Lambda_{eff}}{\Lambda_{eff}}(10^{-6})$
10	3.09	1.04	3.50
25	2.50	1.51	2.80
100	1.58	14.5	17.8
250	3.26	17.4	18.4

Therefore, the residual error is quantified using (i) steady-state convergence diagnostics (residual/stopping criteria and spatial uniformity of the steady heat flux), and (ii) the sensitivity of the extracted closure parameters to the thickness subset ("window") used in the $1/k - 1/L_y$ regression.

At a sample size of $L_y = 100\Delta y$, the steady-state convergence error accounting for the maximum difference in heat flux $Q = Q_y/Q_{y,m}$ and temperature θ between two successive time steps is estimated for a range of $1/\lambda_U$ by selective tolerance to the stopping criterion, Fig. 2. Some entries are treated as zero, as the convergence is achieved within the 64-bit double precision value. As $t/\Delta t \to 10^5$, it can be seen that all the cases converged to non-dimensional residuals below $O(10^{-9})$. Similar observations can be made for all L_y.

To characterize the sensitivity of the extracted closure parameters to the thickness subset, we define a holdout protocol and a window-sensitivity metric. For a given sample dataset with a fixed mixing parameter, we split the available thicknesses L_y into a fit set $\mathcal{L}_{fit}$ and a disjoint test set $\mathcal{L}_{test}$. Using only $\mathcal{L}_{fit}$, we perform the linear regression implied by Eq. (31). In this case, the fit set is $\mathcal{L}_{fit} = \{5, 10, 20, 50, 200, 800\}$, and then, Eq. (30) is used to predict $k(L_y)$ over the held-out thicknesses $\mathcal{L}_{test} = \{4, 6, 7, 8, 16, 25, 100, 500\}$. The corresponding closure parameters are then obtained from the regression coefficients, where the prediction accuracy is quantified over the test set $\mathcal{L}_{test}$ using mean relative error, $\bar{\varepsilon}$.

We also quantify the sensitivity of the extracted closure parameters to the thickness window used in the regression by repeating the fit over multiple thickness subsets ("windows") w, yielding parameter pairs $(k_{LBPC}^{(w)}, \Lambda_{eff}^{(w)})$. Here, we consider four windows: (i) the full thickness set (total 14 values for L_y), (ii) excluding the smallest two L_y, (iii) excluding the largest two L_y, and (iv) six intermediate values of L_y. A compact robustness measure is analyzing the max difference across the windows, non-dimensionalized by the mean values, $\Delta k_{LBPC}/\bar{k}_{LBPC}$ and $\Delta\Lambda_{eff}/\bar{\Lambda}_{eff}$, respectively.

For sample 1 across a range of mixing parameters, Table II reports the mean relative uncertainty in conductivity prediction, as well as windowing uncertainties in closure parameters. It can be seen that the level of error is bounded by $O(10^{-5})$.

III. RESULTS

In this section, we discuss the approach to recover the MSFM closure parameters of effective thermal conductivity, bulk-like

thermal conductivity, effective mean free path, and ballistic thermal conductance from LBPC simulations considering the entirety of the mathematical experiment grid. The results are portrayed for sample 1 material type; however, for the interest of the reader the full dataset is available in supplementary material B: DETAILED DATA. At the end of the results, a comprehensive analytical solution to the steady-state heat conduction problem is presented to demonstrate the effects of ballistic transport in samples smaller than the phonon scattering MFP. It is shown that the steady-state temperature profile (analytical expression) can accurately predict the heat flux upon using the proposed bulk-like thermal conductivity closure rather than the conventional conductivity based on the kinetic theory of phonon gas.

A. Estimation of G_{ball} and C_V from Q_m

For all the LBPC simulations conducted, the highest heat flux values were consistently observed for the pure ballistic limit ($\lambda_U = 0$) of each material type and independent of the sample size. In particular, the maximum heat flux ($Q_{y,m}$) values attained are 20.48, 17.86, 13.16, and 10.37 for samples 1–4, respectively. Normalizing by the nondimensional temperature to attain G_{ball}, and charting with respect to phonon energy ϵ_A^0, an inverse relationship can be observed in Figs. 3(a) and 3(c) consistent with Eq. (28). Similarly, $C_v v_g$ can also be charted as a function of ϵ_A^0, displayed as an inverse correlation in Fig. 3(b). When fitted with a linear regression, G_{ball} and $C_v v_g$ can be estimated as

$$G_{ball} = b_1\left(1 - d_1\epsilon_A^0\right)v_g n_p k_B = \frac{C_v v_g}{4} \text{ and } C_v = 4b_1\left(1 - d_1\epsilon_A^0\right)n_p k_B, \tag{32}$$

with $b_1 = 24.55$, $d_1 = 0.3$, and C_v is the specific heat of the material in then LBPC context. Then, $C_V = C_v T_0$ will be the exact conversion to the real C_V parameter.

B. Steady-state distributions of θ and Q_y

The temperature and heat flux values are also derived directly from the numerical simulations using the input parameters specified in the design of experiments (see Fig. B-1 in the supplementary material for all four samples). For a thickness of $L_y = 100\Delta y$ of sample type 1, Fig. 4 displays the steady-state distributions of the dimensionless temperature θ and heat flux $Q_y(\boldsymbol{r}, t)/Q_{y,m}$. It should be noted that the flux value also varies depending on the sample type, despite identical temperature distributions (shown in Fig. B-1 in the supplementary material), as the variation in thermal diffusivity is determined solely by the reciprocal of the phonon MFP ($1/\lambda_U$), while the heat flux is influenced by both thermal diffusivity and specific heat capacity, which depends on phonon energy. In reality, the heat flux is also size dependent and inversely proportional to the sample thickness (not shown here for brevity). Hence, the thermal conductivity can be determined by utilizing the steady-state heat flux value in relation to the parameter $1/\lambda_U$ and the sample thickness.

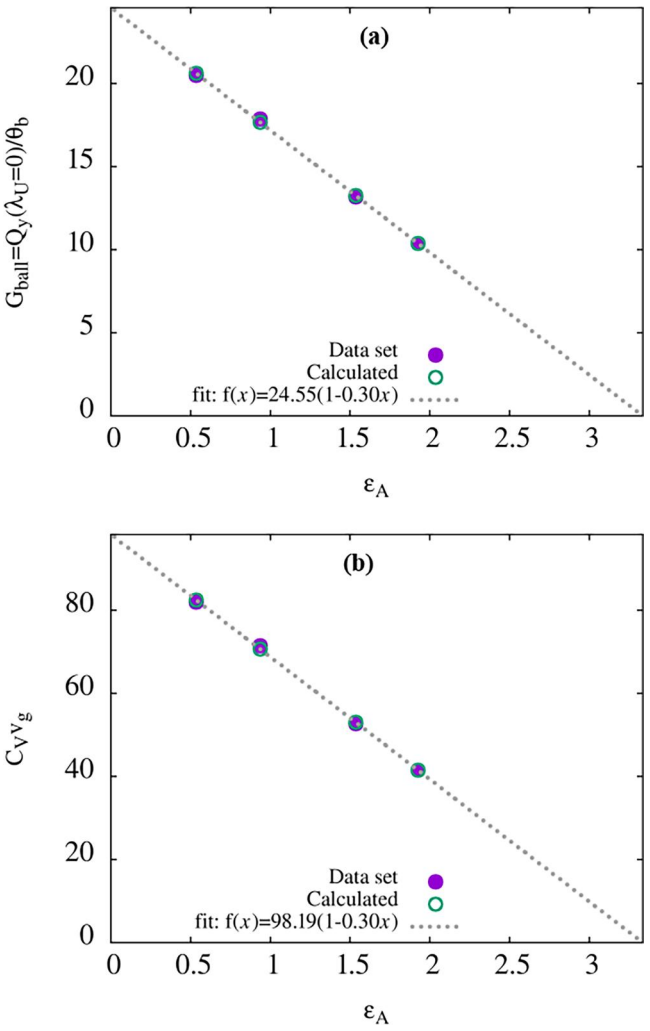

FIG. 3. Ballistic conductance (a) G_{ball} and (b) $C_v v_g$ as a function of phonon energy for all considered material types.

C. Measurements of k from Q_y data

For sample 1 with varying characteristics of $1/\lambda_U$ and sample thickness (L_y), Fig. 5 portrays the steady state Q_y and calculated k. (For all four samples, the comprehensive dataset is presented in Figs. B-2 and B-3 in the supplementary material.) The flux is proportional to $1/\lambda_U$ and inversely proportional to the sample thickness, as indicated by a straight line with a negative slope on the log-log representation. The value of k is heavily influenced by the thickness of the samples, particularly for higher values of $1/\lambda_U$, indicating that the sample thicknesses are significantly smaller than the scattering length of the U-process and the boundary scattering impact on the transport property. For smaller values of $1/\lambda_U$, the system exhibits bulk behavior, and the sample thicknesses exceed the scattering length of the U-process. These results are

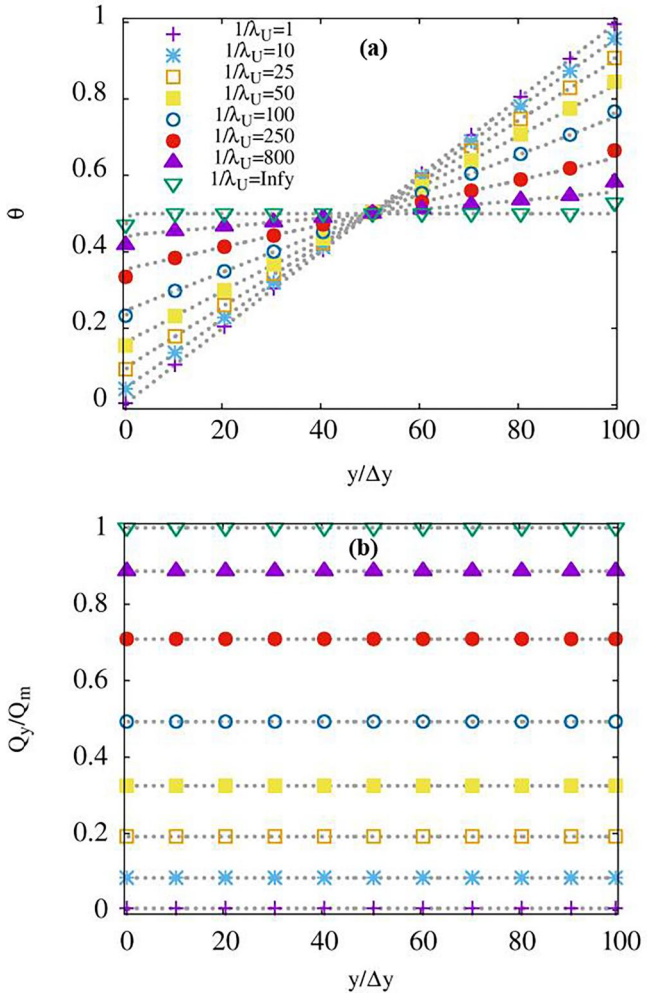

FIG. 4. Steady state distributions of (a) temperature and (b) heat flux of material type sample 1 for a size of $L_y = 100\Delta y$, considering a range of mixing parameters.

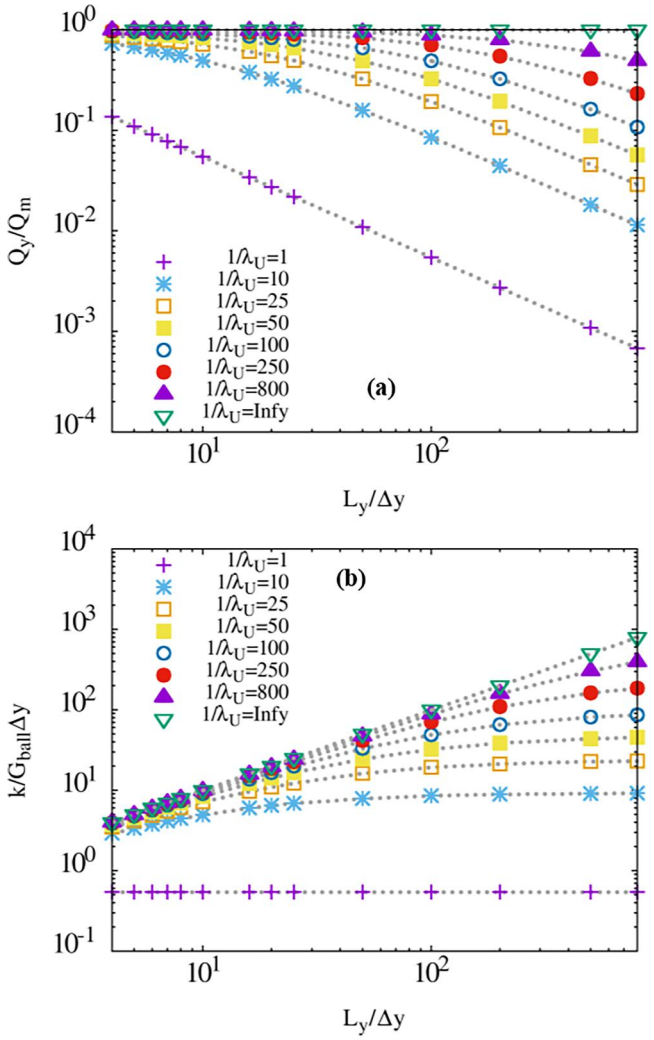

FIG. 5. (a) Steady-state heat fluxes and (b) calculated thermal conductivity of material type sample 1, considering a range of sample size and mixing parameters.

consistent with the experimental and simulated observations from the literature.[19,29–31,59–62]

D. Estimation of Λ_{eff} and k_{LBPC} from $1/k$ vs $1/L_y$ regression

For an imposed pair of mixing parameters of a chosen sample type, the procedure to determine Λ_{eff} and k_{LBPC} involves fitting Eq. (31) with the observed values of k vs L_y. When $1/\lambda_U = 16$, all sample types 1–4 are observed to have the same effective MFP, collapsing to $\Lambda_{eff}/\Delta y = 14.52$ (see Fig. B-4 in the supplementary material for all four types of materials individually). It is true that Λ_U is a valid and convenient definition of the phonon MFP based on the BPC equation via relation $\Lambda_U = \tau_U v_g^{\sigma}$. However, due to the discrete time domain of the LBPC formulation, Λ_U becomes obsolete for small $\tau_U/\Delta t$. In contrast, the effective momentum–relaxation (or attenuation) length is represented by Λ_{eff} for the LBPC formulation. Along these lines, these materials exhibit distinct bulk thermal conductivity values due to their different phonon dispersion relations.

Across a wide range of $1/\lambda_U$ values for the four sample types, Fig. 6 charts (a) phonon MFPs Λ_{eff}/Λ_U and (b) bulk thermal conductivities k_{LBPC} (see Table B-I in the supplementary material for the individual values). In Fig. 6(a), Λ_{eff} decreases significantly at $1/\lambda_U = 1$, leading to an overestimation of the phonon MFP by Λ_U, as τ_U approaches Δt. Λ_{eff} becomes negligible when U-processes dominate over N-processes and boundary scattering; nevertheless, most phonon modes (or the MFP spectrum) primarily determine the non-zero bulk thermal conductivity. On the contrary, the high value of $1/\lambda_U$

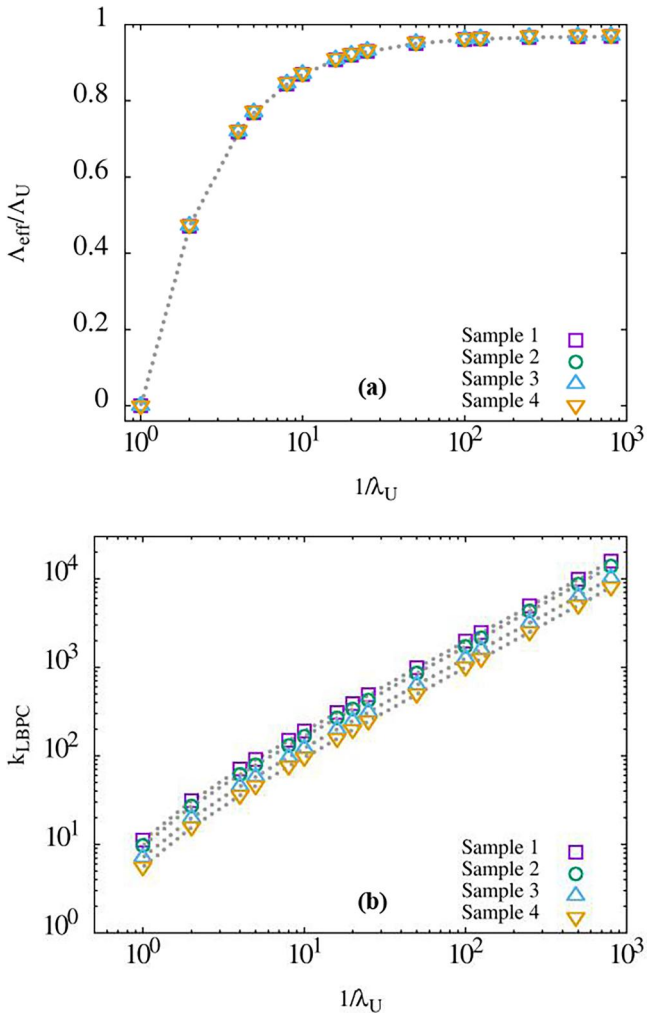

FIG. 6. For all considered material types, (a) effective mean free path and (b) bulk-like thermal conductivity as function of mixing parameter.

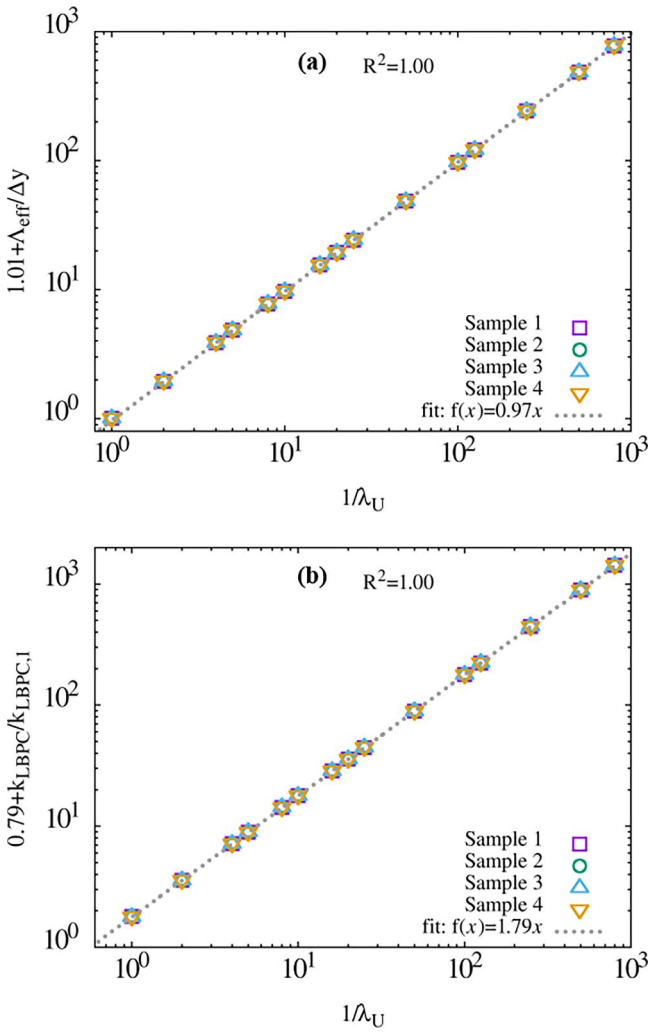

FIG. 7. For all considered material types, linear fit of (a) effective mean free path and (b) bulk-like thermal conductivity as a function of mixing parameter.

indicates that there is an increase in normal phonon scattering, as the effective MFP Λ_{eff} approaches the bulk MFP Λ_U, and consequently, the effective thermal conductivity becomes strongly dependent on Λ_{eff}. In contrast to the portrayed independence of Λ_{eff}/Λ_U to the sample type [Fig. 6(a)], the lines of bulk-like thermal conductivity vs the mixing parameter $1/\lambda_U$ present different slopes for the various phonon energy pairs [Fig. 6(b)], attributed to the changes in the volumetric specific heat capacity of the materials.

E. Models of Λ_{eff}, k_{LBPC}, and k for mesoscale systems

Figure 7(a) charts the data points for Λ_{eff} against $1/\lambda_U$, where the linear fit is approximated as

$$\Lambda_{eff} = \left(\frac{0.97}{\lambda_U} - 1.01\right)\Delta y \approx \left(\frac{1}{\lambda_U} - 1\right)\Delta y = (1-\lambda_U)\Lambda_U. \quad (33)$$

In the case of k_{LBPC} as a function of $1/\lambda_U$, the values are normalized with respect to the reference $k_{LBPC,1}$, representing the diffusive limit ($\lambda_U = 1$) for a given sample type, Fig. 7(b). Then, the linear fit can be approximated as

$$\begin{aligned} k_{LBPC} &= \left[1 + a\left(\frac{1}{\lambda_U} - 1\right)\right] c_0 \Delta y v_g n_p k_B, \\ k_{LBPC} &= \frac{a_0}{\lambda_U}\, k_{LBPC,1};\ a_0 = \lambda_U + a(1-\lambda_U), \end{aligned} \quad (34)$$

where $a = 1.79 \approx 9/5$, which is the same as obtained in the GK model for pure phonon transport.[26]

From Eq. (34), it can be seen that $k_{LBPC,1} = c_0 \Delta y v_g n_p k_B$ and corresponds to numerical values of 11.13, 9.71, 7.14, and 5.65 for

samples 1–4, respectively, which is charted in Fig. 8 as a function of ϵ_A^0 and G_{ball}. Then, the linear fit can be approximated as

$$k_{LBPC,1} = b_2\left(1 - d_2\epsilon_A^0\right)v_g\Delta y n_p k_B = \frac{\Delta y}{a}\frac{C_v v_g}{4} = \frac{G_{ball}\Delta y}{a}, \quad (35)$$

where $b_2 = 13.34$ and $d_2 = 0.3$. Comparing the results from this diffusive limit fitted expression with respect to the ballistic limit fits in Eq. (32), it can be seen that the forms of the equation are identical with a factor of $\Delta y/a$, with the observation that $b_2 = b_1/a = 0.54b_1$ and $d_2 = d_1$. Therefore, to model bulk-like thermal conductivity, k_{LBPC}, Eqs. (34) and (35) can be used with a known specific heat C_v and the factor $1/a$, which is now observed to represent the effects of additional spatial dimensions, geometry, and shape.

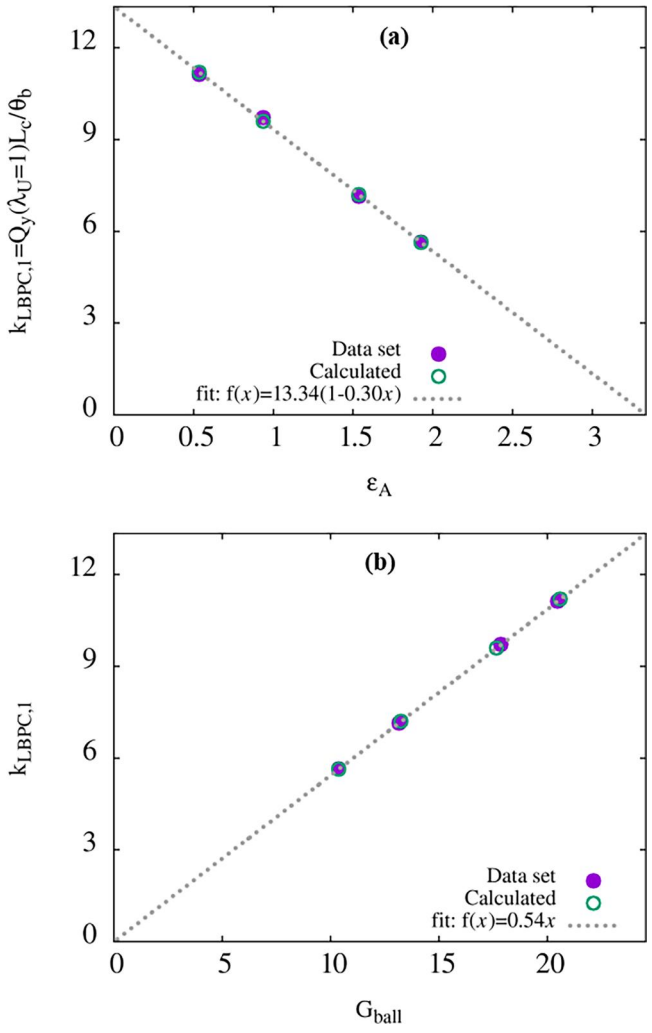

FIG. 8. For all considered material types, models of bulk-like thermal conductivity in the diffusive limit as a function of (a) energy of the phonon and (b) ballistic thermal conductance.

The final of k_{LBPC} can now be given as

$$k_{LBPC} = \frac{a_0}{a}G_{ball}\Lambda_U = b_0 G_{ball}\Lambda_U, \quad (36)$$

where $b_0 = a_0/a = \lambda_U/a + (1-\lambda_U) = 0.54\lambda_U + (1-\lambda_U)$. The prescribed function k_{LBPC} closely resembles the bulk thermal conductivity k_{bulk}, as defined in the MSFM framework using the kinetic theory of phonon gas in the diffusive limit.[5,65] It means for thick samples at the diffusive limit (where $\lambda_U = 1$ and $\Delta y = \Lambda_U$), $k_{LBPC}(\lambda_U = 1) = k_{diff}$, which is also identical to k_∞ when the G_{ball} of Eq. (36) is identical to the G_0 of Eq. (6). Moreover, k_{bulk} becomes infinite if $\lambda_U = 0$, because $\Lambda_U \to \infty$. The additional contribution $(1-\lambda_U)G_{ball}\Lambda_U$ to the bulk thermal conductivity k_{LBPC} arises from the hydrodynamical or viscous behavior of the phonon gas in solid crystals.[19,26,29]

Lastly, by combining Eqs. (30), (33), and (36), a final expression can be written relating the effective thermal conductivity k of a sample with defined properties of phonon energy pair, mixing parameter, and thickness (ϵ_A^0, $1/\lambda_U$, L_y),

$$k(\lambda_U, L_y) = \frac{b_0 G_{ball}\Lambda_U L_y}{L_y + (1-\lambda_U)\Lambda_U}. \quad (37)$$

Now, comparing this form of the effective thermal conductivity to the MSFM framework presented in Eq. (20), $k \equiv k_{eff} = k_{diff}R + k_{ball}\Gamma$ and $k_{LBPC} \equiv k_{bulk} = k_{diff} + G_{ball}\Lambda_{eff}$, where the equivalent terms can be identified from Eq. (37), as $k_{diff} = G_{ball}\Lambda_U/a$, $k_{ball} = G_{ball}L_y$, $\Gamma = (1-\lambda_U)/[\lambda_U L_c + (1-\lambda_U)]$, and $R = \lambda_U L_c/[\lambda_U L_c + (1-\lambda_U)]$. Note that the additional contribution $G_{ball}\Lambda_{eff} = (1-\lambda_U)G_{ball}\Lambda_U$ in k_{LBPC} is due to the hydrodynamical or viscous behavior of the phonon gas transmitting through the medium in solid crystals.[19,26,29]

In the following, the ratio of the effective thermal conductivity to its bulk value can be found from the following expression:

$$\frac{k}{k_{LBPC}}(\lambda_U, \mathrm{Kn}) = \frac{1}{[1 + (1-\lambda_U)\mathrm{Kn}]}. \quad (38)$$

Note that the condition beyond $0 \le \lambda_U \le 1$ and $\lambda_U < 0$ is not possible in the present formulation because the quantity Λ_{eff}/Λ_U would become either less than zero (if $\lambda_U > 1$) or greater than one (if $\lambda_U < 0$). However, when the findings of Majumdar[5] are expressed in our form, $1-\lambda_U = 4/3$ expression can be recovered, and combining it with Eq. (38), the k/k_∞ ratio can be written as

$$\left(\frac{k}{k_\infty}\right)_{\text{Majumdar}} = \frac{1}{1 + \frac{4}{3}\mathrm{Kn}}. \quad (39)$$

Similarly for the gray models,[101] our form recovers $1-\lambda_U = 2C$, and by choosing the geometric parameter $C = 1$, the expression for

k/k_∞ becomes

$$\left(\frac{k}{k_\infty}\right)_{\text{gray}} = \frac{1}{1+2\text{Kn}}. \tag{40}$$

Charting the k/k_{LBPC} expression outlined in Eq. (38) with respect to Kn, Fig. 9 presents the solution for differing ballistic and diffusive extremes (black and red dashed lines, respectively), an intermediate case of $1/\lambda_U = 1.25$ (green dashed line), as well as prior models (gray[101] and Majumdar[5] represented by solid lines). The discrete simulation datapoints (k/k_{LBPC} vs Kn) are not included in Fig. 9 for clarity and can be found in supplementary material B: Detailed data (see Table B-II in the supplementary material for discrete values of Kn and k/k_{LBPC} in both Table B-III and Fig. B-5 in the supplementary material). Note that the thermal conductivity ratio is constant and equal to unity at the diffusive limit $Kn \ll 1$, whereas the ballistic limit is length dependent and asymptotically goes to zero, as $Kn \gg 1$. The shape of the normalized tendencies of the present and previous models (k/k_{LBPC} and k/k_{bulk} vs Kn) may seem similar; however, the reference values k_{LBPC} and k_{bulk} are quite different. k_{bulk} is a function of temperature only for infinitely long samples at the diffusive limit, whereas k_{LBPC} is a function of temperature and diffusive–ballistic mixing parameters. Therefore, note that k_{LBPC} and k_{bulk} are identical only for the diffusive process across infinitely long samples. Considering that the normalized trends are similar, the historic challenge in estimating accurate conductivity values seems to arise from an ambiguity in adequately defining k_{LBPC}.

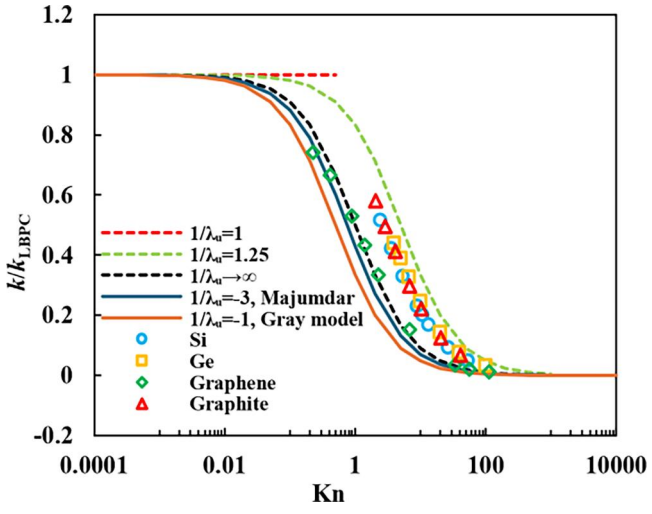

FIG. 9. Ratio of thermal conductivity to bulk-like thermal conductivity as a function of Knudsen number at differing values of the mixing parameter. Existing gray[101] and Majumdar[5] models are indicated by solid lines (orange and blue, respectively). Literature data for various materials (Si and Ge from Refs. 46 and 47, graphene from Refs. 17 and 18, and graphite Ref. 31) are shown in markers.

To validate the proposed closure against the existing measurements from the literature, we compile datasets using predicted values of k_∞ and Umklapp phonon scattering length, Λ_U, for various materials: Si ($k_\infty = 150$ W/m K, $\Lambda_U = 268$ nm) and Ge ($k_\infty = 60$ W/m K, $\Lambda_U = 198$ nm) from Refs. 46 and 47, graphene ($k_\infty = 3200$ W/m K, $\Lambda_U = 1700$ nm) from Refs. 17 and 18, and graphite ($k_\infty = 7$ W/m K, $\Lambda_U = 204$ nm) from Ref. 31. Figures B-6(a)–B-6(d) in the supplementary material chart show the $1/k$ vs $1/L_y$ data from the literature for all the materials, along with the best fit curves. Then, the fits are resampled for discrete values of k and L_y and the results are presented in Fig. 9 with the relevant markers (the exact values are provided in Table B-IV in the supplementary material).

Evidently, the data from the literature fall between the bounds of our ballistic–diffusive predictions. The slight potential deviation in graphene arises from the lack of the exact established bulk reference value. Then, for each k_∞ and Λ_U pair, the bulk-like conductivity, effective MFP and mixing parameters can be computed from the regression (provided in Table B-V in the supplementary material). All samples indicated $0 < \lambda_U < 1$, which reflects the non-diffusive transport nature of these real samples.

F. Heat conduction with jump BCs and steady-state solution

Having established constitutive relations from LBPC that are compatible with the MSFM framework, the steady-state heat conduction problem can be solved, assuming that the backscattering length Λ_b in the MSFM is equal to the effective phonon MFP Λ_{eff} in LBPC, i.e., $\Lambda_b = \Lambda_{\text{eff}} = (1-\lambda_U)\Lambda_U$, and equitable transfer fractions Γ and R.

Moreover, the steady-state BC jumps are $\theta(y_L) = \theta_L + \Gamma\theta_b/2$ and $\theta(y_R) = \theta_R - \Gamma\theta_b/2$, for the left wall and right wall, respectively, where $\theta_b = (\theta_R - \theta_L)$ and defines the quantity $\theta_M - \theta_P = (1-\Gamma)\theta_b = \text{R}\theta_b$. The steady-state problem (in the discrete domain $y \to y/\Delta y$, $L_c \to L_y/\Delta y$) can be represented as

$$\frac{d^2\theta}{dy^2} = 0, \tag{41}$$

subjected to the Dirichlet BCs $\theta(y_L) = \theta_P$ and $(y_R) = \theta_M$ or jump BCs,

$$-\frac{(1-\lambda_U)}{2}\left(\frac{d\theta}{dy}\right)_{y_L} + \lambda_U\theta\big|_{y_L} = \lambda_U\theta_L \text{ and } \frac{(1-\lambda_U)}{2}\left(\frac{d\theta}{dy}\right)_{y_R} + \lambda_U\theta\big|_{y_R} = \lambda_U\theta_R, \tag{42}$$

using $\Lambda_b = \Lambda_{\text{eff}} = (1-\lambda_U)\Lambda_U$ and $\lambda_U = \Delta y/\Lambda_U$.

These expressions in Eq. (42) represent the jump BC for a mesoscale heat transfer problem due to transmission and backscattering of the phonon within the medium. Then, the solution for the temperature θ is given by

$$\theta(y) = \theta_P + (\theta_M - \theta_P)\frac{(y-y_L)}{L_c} = \theta_P + \text{R}\frac{(y-y_L)\theta_b}{L_c} = \theta_m + \frac{\lambda_U(y-y_m)\theta_b}{[\lambda_U L_c + (1-\lambda_U)]}, \tag{43}$$

where $\theta_m = \theta_L + \Delta\theta_b/2$, $y_m = y_L + L_c/2$, and $L_c = (y_R - y_L)$. The length dependent temperature profile within the medium is an outcome of the reflected/backscattered phonons. The corresponding temperature gradient induced heat flux $Q_y(y)$ is given by

$$Q_y(y) = -\frac{k\theta_b}{L_c} = Q_{y,d} + Q_{y,b}, \tag{44}$$

where $Q_{y,d} = -k_{\text{diff}}(d\theta/dy) = -k_{\text{diff}}\lambda_U\theta_b/[\lambda_U L_c + (1-\lambda_U)]$ is the diffusive component and $Q_{y,b} = G_{\text{ball}}\Delta\theta = -(1-\lambda_U)G_{\text{ball}}\theta_b/[\lambda_U L_c + (1-\lambda_U)]$ is the ballistic component. The overall diffusive-ballistic heat flux $Q_y(y)$ can be expressed as

$$Q_y(y) = -(k_{\text{diff}}\mathrm{R} + G_{\text{ball}}L_c\Gamma)\frac{\theta_b}{L_c} = -\frac{k_{\text{LBPC}}\lambda_U L_c}{[\lambda_U L_c + (1-\lambda_U)]}\frac{\theta_b}{L_c}, \tag{45}$$

where $k_{\text{LBPC}} = b_0 G_{\text{ball}}\Lambda_U = b_0 G_{\text{ball}}\Delta y/\lambda_U$ is the bulk thermal conductivity and $k = (G_{\text{ball}}\Lambda_U/a)\mathrm{R} + G_{\text{ball}}L_y\Gamma = b_0 G_{\text{ball}}L_c/[\lambda_U L_c + (1-\lambda_U)]$ is the effective thermal conductivity, which incorporates the effects from both effective MFP $(1-\lambda_U)\Lambda_U$ and Kn $(= 1/\lambda_U L_c)$ of the system after replacing $\Lambda_U = \Delta y/\lambda_U$.

For sample 1, the comparison between temperature profiles and heat fluxes of the steady state solutions based on the direct LBPC formulation and the analytical solutions based on the MSFM in Eqs. (43)–(45), are presented in Figs. 10(a) and 10(b), respectively. The two methods show quantitative consistency across different diffusive and ballistic regimes, indicating that the closure parameters are identified and translated in a consistent manner. Considering that the differential equation of the Fourier model can be derived from the MSFM framework in the steady state, this work suggests that the Fourier model, incorporated with the jump BC and bulk-like thermal conductivity, can be used to adequately capture the mesoscale effects as well.

IV. DISCUSSION

The results clarify the physical interpretation of effective thermal conductivity in the ballistic–diffusive regime and the conditions under which mesoscale transport can be represented by reduced constitutive descriptions. Although ballistic–diffusive transitions are often parameterized using the *Knudsen* number (Kn), the present analysis shows that Kn-based descriptions are incomplete unless the relevant scattering lengths and their relation to sample geometry and boundary backscattering are explicitly considered. Away from the diffusive and infinite sample size limit, the effective thermal conductivity is, therefore, not an intrinsic bulk material property; it is a system-level response governed by resistive scattering, finite thickness, and induced backscattering.

A central outcome of this study is an analytical decomposition of the heat flux within the extended MSFM framework into ballistic and diffusive contributions, which provides a transparent mesoscale description of the net transport as the superposition of forward-propagating and backscattered phonons. While flux-based descriptions exist in earlier MSFM models, the present contribution is a mesoscale thermal law through which these contributions are expressed in terms of ballistic thermal conductance, backscattering length, sample size, and bulk-like thermal conductivity.

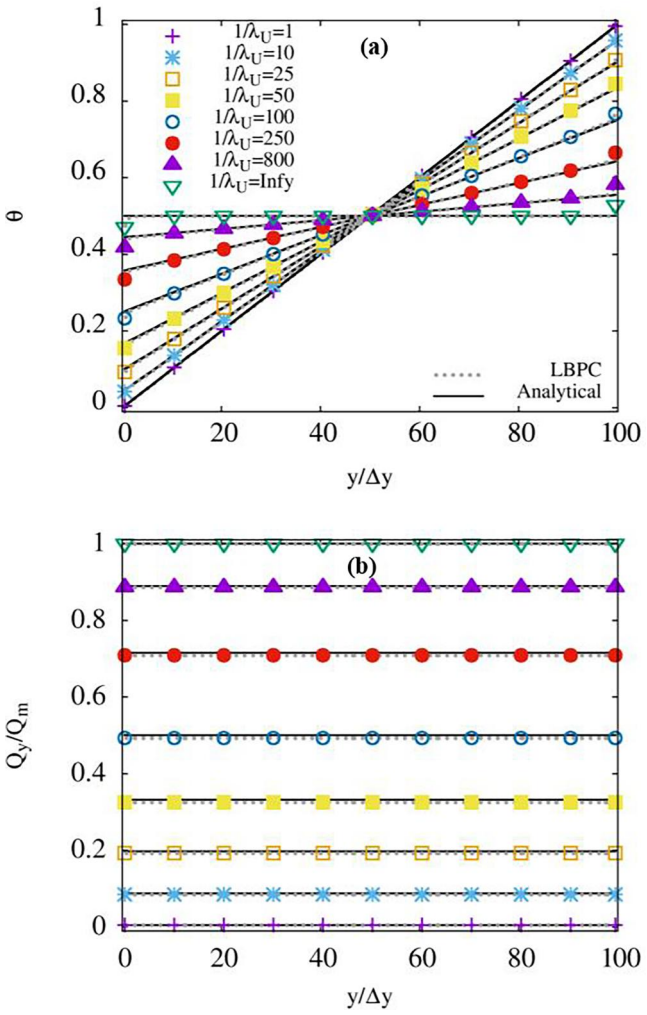

FIG. 10. LBPC formulation (dotted with markers) and MSFM derived analytical expressions [provided in Eqs. (45)–(47)] (indicated in solid lines) comparison, using steady-state distributions of (a) temperature and (b) heat fluxes of material type sample 1 for a size of $L_y = 100\Delta y$, considering a range of mixing parameters.

LBPC plays a complementary role by providing an independent route to identify the closure parameters required by the MSFM. Systematic steady-state LBPC thickness sweeps yield temperature fields and heat fluxes from which an effective phonon MFP and an LBPC-defined bulk-like thermal conductivity are extracted through the conductivity vs thickness regression. The collapse of the normalized thermal-conductivity results from the present LBPC simulations, existing models, and representative literature data for silicon, germanium, graphene, and graphite onto a common trend supports the applicability of the identified closure parameters over the range examined. Using this regression to close the MSFM relations provides an opportunity to reduce the degrees of freedom in the model.

Within this closed framework, the MSFM backscattering length can be interpreted as an effective resistive (attenuation) length governing ballistic–diffusive mixing in finite domains. This interpretation explains why effective thermal conductivity depends primarily on scattering length to thickness scaling and why conductivity curves organized solely by Kn do not generally collapse when the underlying resistive length scales and boundary backscattering differ across materials maintained at different temperatures (i.e., dissimilar DOS for phonons).

More broadly, the results clarify why classical continuum closures (analytical frameworks such as Fourier, CV, DPL, and GK) are inadequate in regimes where boundary scattering and nonlocality are significant, considering that they rely on bulk transport coefficients, defined in the diffusive infinite sample size limit, and do not explicitly account for mesoscale effects in their original form. In contrast, the MSFM–LBPC framework retains the kinetic information needed to construct such a closure while remaining analytically tractable and computationally efficient.

V. CONCLUSIONS

We developed a closed mesoscale constitutive description for ballistic–diffusive heat transport by extending the *McKelvey–Shockley* Flux Method (MSFM), deriving an explicit ballistic–diffusive flux decomposition, and identifying the required closure parameters: a ballistic thermal conductance, an effective backscattering length, and a bulk-like thermal conductivity. The ballistic thermal conductance is dictated by material properties. The backscattering length, which governs the dynamics of the transport, and the bulk-like thermal conductivity are modeled by a new framework based on independent steady-state Lattice–*Boltzmann–Peierls–Callaway* (LBPC) simulations for different materials, thicknesses, and ballistic–diffusive mixing parameters. Then, the MSFM yields a closed mesoscale thermal law, for a given Knudsen number.

SUPPLEMENTARY MATERIAL

See the supplementary material for details on (a) models of MSFM and LBPC, and (b) data and plots in SUPPLEMENTARY A: MODELS and SUPPLEMENTARY B: DETAILED DATA, respectively.

ACKNOWLEDGMENTS

This presents research effort has received funding from the European Research Council (ERC) under the European Union's Horizon 2020 Research and Innovation Programme (Grant Agreement No 853096—ThermoTON). The LBPC code is developed as a modification of *Tony Ladd*'s Susp3D[123] (a hybrid MD and LB software package under GNU public license) by *J. Lee* and *A. K. Roy*.[83]

NOMENCLATURE

A_i^σ	Directional equilibrium distribution function, $A_i^\sigma = 1/(e^{\beta_0\epsilon_i^\sigma} - 1)$
a	Numerical value, $a = 1.79 \approx 9/5$
a_0	A parameter defined as $a_0 = \lambda_U + a(1-\lambda_U) = \lambda_U + 1.79(1-\lambda_U)$
b_0	A parameter defined as $b_0 = a_0/a = \lambda_U/a + (1-\lambda_U) = 0.54\lambda_U + (1-\lambda_U)$
B_i^σ	A factor defined as $B_i^\sigma = -e^{\beta_0\epsilon_i^\sigma}/(e^{\beta_0\epsilon_i^\sigma} - 1)^2 = \partial A_i^\sigma/\partial\beta_0\epsilon_i^\sigma = -A_i^\sigma(1 + A_i^\sigma)$
c	Speed of the lattice *Boltzmann* method (LBM) code, $c = v_g$ in the present consideration
$\boldsymbol{c}_i$	Velocity vector connecting the lattice node at $\boldsymbol{r}$ with the neighboring node at $\boldsymbol{r} + \boldsymbol{c}_i\Delta t'$
C_V	Specific heat (J/m^3 K), $C_V = \partial e/\partial T = 16\sigma T_0^3/v_g$
C_v	Specific heat equivalence in LBPC ($n_p k_B$), $C_v = 4b_1(1 - d_1\epsilon_A^0)n_p k_B$
$DdQq$	Configuration of LBM with lattice having d–dimensions and q-points, such as $D3Q19$
d	Derivative
D	Density of states, for phonons $D(\epsilon) = 12\pi\epsilon^2/(hv_g)^3$
D_{ph}	Phonon diffusivity, $D_{ph} = \Lambda_b v_y^+/2$ (traditionally $\Lambda_U v_g/3$)
$e(\boldsymbol{r}, t)$	Energy density (J/m^3), $e = (q^+ + q^-)/v_y^+ = C_V T$
$\vec{e}_i$	Direction in LBM formulation
$E(\boldsymbol{r}, t)$	Total energy density in LBPC [($n_p k_B T_0$), J/m^3]
f^σ	Single phonon distribution function
f_i^σ	Directional phonon number distribution function
$f_i^{*\sigma}$	Directional postcollision phonon number distribution function [(n_p), 1/m^3]
f(x)	Function of variable x while fitting numerical data
G_0	Ballistic thermal conductance per unit area (W/m^2 K), $G_0 = C_V v_y^+/2 = C_V v_g/4$
G_{ball}	Equivalence of G_0 in LBPC ($v_g n_p k_B$), $G_{ball} = b_1(1 - d_1\epsilon_A^0)v_g n_p k_B = C_v v_g/4$
h	*Planck*'s constant (J s)
$\mathbf{k}$	Phonon wave vector with magnitude k
k	Thermal conductivity [($v_g \Delta y n_p k_B$), W/m K], $k = C_V D_{ph} = G_0\Lambda_b$ (traditionally $G_0 4\Lambda_U/3$)
k_B	*Boltzmann* constant (J/K)
Kn	*Knudsen* number, defined as Kn = $\Lambda_U/L_y = 1/\lambda_U L_c$
L_c	Length of the sample in the y direction in the unit of Δy, $L_c = L_x/\Delta y$
L_x, L_y, L_z	Length of the sample in x, y, and z directions, respectively
M	Atomic or molecular mass
n_p	Phonon density, $n_p = N_p/V = N_A\rho_m/M$ (1/m^3)
N_p	Total number of phonons in volume V
N_A	*Avogadro*'s number
$\mathbf{p}$	Phonon momentum, $\hbar\mathbf{k}$
$\mathbf{p}_i^\sigma$	Directional phonon momentum with magnitude p, $\mathbf{p}_i^\sigma = p\vec{e}_i$
$\boldsymbol{P}(\boldsymbol{r}, t)$	Total momentum density [($n_p k_B T_0/v_g$), N s/m^3]
$\boldsymbol{q}$	Heat flux (W/m^2), $q = q^+ - q^-$
$\boldsymbol{q_m}$	Maximum heat flux (W/m^2)
$q^\pm$	Directional heat flux, $q^\pm = G_0 T^\pm$
$\boldsymbol{Q}(\boldsymbol{r}, t)$	Normalized heat flux, $\boldsymbol{q}/\boldsymbol{q_m}$
$\boldsymbol{Q_y}(\boldsymbol{r}, t)$	Total heat flux obtained in LBPC ($v_g n_p k_B T_0$)
$\boldsymbol{Q_{y,m}}(\boldsymbol{r}, t)$	Maximum heat flux obtained in LBPC ($v_g n_p k_B T_0$)
R	Reflection fraction within materials due to backscattering, R = $1 - \Gamma = L_y/(\Lambda_b + L_y)$
$\boldsymbol{r}$	Central node at $\boldsymbol{r}$ in LBM

$\Delta \boldsymbol{r}$	Neighbor node of $\boldsymbol{r}$ connected via $\boldsymbol{r}+\boldsymbol{c}_i\Delta t'$ in LBM, $\Delta \boldsymbol{r}_i = \boldsymbol{c}_i \Delta t'$
t	Time (s)
Δt	Time step in LBM
$\Delta t'$	Update time of f_i^σ in the unit of Δt, $\Delta t' = (v_g^\sigma/c)\Delta t = \Delta t/(1+\sigma)$
$T(\boldsymbol{r}, t)$	Temperature (K)
$T^\pm$	Directional temperature, $T^\pm = q^\pm/\mathrm{G}_0$
T_0	Initial temperature (K)
$\mathbf{u}(t, \boldsymbol{r})$	Local drifting velocity conjugate to the crystal momentum $\hbar\mathbf{k}$
$\tilde{\mathbf{u}}(\boldsymbol{r}, t)$	Perturbation of phonon drift velocity, $\tilde{\mathbf{u}}(\boldsymbol{r}, t) = (\mathbf{u}(\boldsymbol{r}, t) - \mathbf{u}_0)/v_g$
v_g	Intrinsic group velocity of the LA phonon (m/s), $v_g = \epsilon/p$
$\mathbf{v}_{g\mathbf{k}}^\sigma$	Group velocity of phonon with polarization σ
$\mathbf{v}_{i,g}^\sigma$	Directional group velocity of the polarized phonon, $\mathbf{v}_{i,g}^\sigma = v_g^\sigma \vec{e}_i$
v_g^σ	Magnitude of $\mathbf{v}_{i,g}^\sigma$, $v_g^\sigma = v_g/(1+\sigma)$
v_y^+	Thermal speed of phonons (m/s), $v_y^+ = \sqrt{D_{ph}/\tau_Q} = v_g/2$ (traditionally $v_g/\sqrt{3}$)
V	Volume of the domain considered (m^3), $V = L_x L_y L_z$
x, y, z	Cartesian coordinates
$\Delta x, \Delta y, \Delta z$	Lattice spacing in LBM in x, y, and z directions, respectively, $\Delta x = \Delta y = \Delta z = c\Delta t$
z_i	Square of length of directional vector $\vec{e}_i$, $z_i = \lvert\vec{e}_i\rvert^2$
Z	Valency of the atom or molecule

Greek letters

δ	Deviational
∂	Partial derivative
$\beta(\boldsymbol{r}, t)$	Local temperature, $1/k_B T$
Γ	Transmission fraction within the material due to transmission, $\Gamma = \Lambda_b/(\Lambda_b + L_y)$
Δ	Difference
ϵ	Intrinsic phonon energy
ϵ_i^σ	Energy of polarized phonon, $\epsilon_i^\sigma = \epsilon_i/(1+\sigma) = z_i\epsilon/(1+\sigma)$
$\theta(\boldsymbol{r}, t)$	Perturbations of the temperature $(\beta_0 - \beta)/\beta = (T(\boldsymbol{r}, t) - T_0)/T_0$
λ	Mixing parameters, $\lambda_{U[N]} = \Delta y/\Lambda_{U[N]}$
Λ	Mean free path (m), $\Lambda = \tau v_g$
Λ_b	Backscattering length (m), $\Lambda_b = \tau_b v_y^+ = \tau_Q v_g$ (traditionally $4\Lambda_U/3$)
$\mathcal{L}$	Length set for the closure and sensitivity analysis of parameters
ρ_m	Density of material ($\mathrm{kg/m}^3$)
σ	Polarization index of phonon, 0 for LA and 1 TA phonons
σ_e	Electrical conductivity of conductors, $\sigma_e = n_e e^2 \tau_e/m_e$
σ_{SB}	*Stefan–Boltzmann* constant ($\mathrm{W/m^2\,K^4}$), $\sigma_{SB} = \pi^5 k_B^4/5h^3 v_g^2$
τ	Relaxation time (s)
τ_b	Backscattering time (s), $\tau_b = \Lambda_b/v_y^+$ (traditionally $8\tau_U/3$)
τ_Q	Thermal relaxation time (s), $\tau_Q = \Lambda_b/2v_y^+$ (traditionally $4\tau_U/3$)
ω	Angular frequency (Hz)
ω_i^σ	Directional weight factor such that $f_{i,0}^{\sigma,eq} = \omega_i^\sigma A_i^\sigma$
$\hbar$	*Planck*'s modified constant (J s/rad)

Subscripts and superscript

–	Bar indicates the mean value
0	Initial value, ballistic value
∞	At diffusive limit
σ	Polarization index of phonon, 0 for LA and 1 TA phonons
A	Acoustic
ball	Ballistic limit
BE	Bose–Einstein
bulk	Bulk
b	Ballistic
c	Combined
d	Diffused, displaced
diff	Diffusive limit
err	Error
eq	Equilibrium
eff	Effective
fit	Fitted
g	Group
i	ith direction in LBM, ith grid point y direction
L	Left
m, max	Maximum
min	Minimum
Mean	Mean or average value
N	Normal
O	Optical
p, ph	Phonon
pre	Predicted
R	Right
RE	Residual/relative error
test	Tested
U	Umklapp
w	Window
y	y direction

Abbreviations

BPC	Boltzmann–Peierls–Callaway equation
BTE	Boltzmann transport equation
CV	Cattaneo and Vernotte
DPL	Dual-phase lag
GK	Guyer–Krumhansl
LA	Longitudinal acoustic
LBM	Lattice Boltzmann method
LBPC	Lattice Boltzmann–Peierls–Callaway equation
MFP	Mean free path
MSFM	McKelvey–Shockley flux method
RE	Relative error
TA	Transversal acoustic

AUTHOR DECLARATIONS

Conflict of Interest

The authors have no conflicts to disclose.

Author Contributions

P. Biswas: Conceptualization (equal); Data curation (equal); Formal analysis (equal); Investigation (equal); Methodology (equal); Software (equal); Validation (equal); Visualization (equal); Writing – original draft (equal); Writing – review & editing (equal). **J. Lee:** Investigation (equal); Methodology (equal); Software (equal); Writing – review & editing (equal). **A. Roy:** Methodology (equal); Software (equal). **B. Cukurel:** Conceptualization (equal); Formal analysis (equal); Funding acquisition (equal); Investigation (equal); Methodology (equal); Resources (equal); Supervision (equal); Validation (equal); Visualization (equal); Writing – original draft (equal); Writing – review & editing (equal).

DATA AVAILABILITY

The data that support the findings of this study are available in the supplementary material.

REFERENCES

[1]J. W. Lynn, H. G. Smith, and R. M. Nicklow, "Lattice dynamics of gold," Phys. Rev. B **8**(8), 3493–3499 (1973).
[2]H. Bilz and W. Kress, *Phonon Dispersion Relations in Insulators* (Springer, Berlin, 1979), Vol. 10.
[3]ÉD Murray, S. Fahy, D. Prendergast, T. Ogitsu, D. M. Fritz, and D. A. Reis, "Phonon dispersion relations and softening in photoexcited bismuth from first principles," Phys. Rev. B **75**(18), 184301 (2007).
[4]D. Lacroix, I. Traore, S. Fumeron, and G. Jeandel, "Phonon transport in silicon, influence of the dispersion properties choice on the description of the anharmonic resistive mechanisms," Eur. Phys. J. B **67**(1), 15–25 (2009).
[5]A. Majumdar, "Microscale heat conduction in dielectric thin films," J. Heat Transfer **115**(1), 7–16 (1993).
[6]A. A. Joshi and A. Majumdar, "Transient ballistic and diffusive phonon heat transport in thin films," J. Appl. Phys. **74**(1), 31–39 (1993).
[7]P. Kim, L. Shi, A. Majumdar, and P. L. McEuen, "Thermal transport measurements of individual multiwalled nanotubes," Phys. Rev. Lett. **87**(21), 215502 (2001).
[8]S. Torii and W.-J. Yang, "Heat transfer mechanisms in thin film with laser heat source," Int. J. Heat Mass Transf. **48**(3–4), 537–544 (2005).
[9]J. Ordonez-Miranda *et al.*, "Anomalous thermal conductivity by surface phonon-polaritons of polar nano thin films due to their asymmetric surrounding media," J. Appl. Phys. **113**(8), 084311 (2013).
[10]L. Zeng *et al.*, "Measuring phonon mean free path distributions by probing quasiballistic phonon transport in grating nanostructures," Sci. Rep. **5**(1), 17131 (2015).
[11]Y. Guo and M. Wang, "Phonon hydrodynamics and its applications in nanoscale heat transport," Phys. Rep. **595**, 1–44 (2015).
[12]G. Chen, "Non-Fourier phonon heat conduction at the microscale and nanoscale," Nat. Rev. Phys. **3**(8), 555–569 (2021).
[13]K. Ghosh, A. Kusiak, and J.-L. Battaglia, "Phonon hydrodynamics in crystalline materials," J. Phys.: Condens. Matter **34**(32), 323001 (2022).
[14]W. Liu and M. Asheghi, "Phonon–boundary scattering in ultrathin single-crystal silicon layers," Appl. Phys. Lett. **84**(19), 3819–3821 (2004).
[15]B. Thouy, J. P. Mazellier, J. C. Barbe, and G. Le Carval, "Phonon transport in electronic devices: From diffusive to ballistic regime," in *2008 International Conference on Simulation of Semiconductor Processes and Devices* (IEEE, 2008), pp. 285–288.
[16]E. Pop and K. E. Goodson, "Thermal phenomena in nanoscale transistors," J. Electron. Packag. **128**(2), 102 (2006).
[17]E. Pop, V. Varshney, and A. K. Roy, "Thermal properties of graphene: Fundamentals and applications," MRS Bull. **37**(12), 1273–1281 (2012).
[18]X. Xu *et al.*, "Length-dependent thermal conductivity in suspended single-layer graphene," Nat. Commun. **5**(1), 3689 (2014).
[19]M.-H. Bae *et al.*, "Ballistic to diffusive crossover of heat flow in graphene ribbons," Nat. Commun. **4**(1), 1734 (2013).
[20]A. J. Minnich *et al.*, "Thermal conductivity spectroscopy technique to measure phonon mean free paths," Phys. Rev. Lett. **107**(9), 095901 (2011).
[21]A. J. Minnich, "Advances in the measurement and computation of thermal phonon transport properties," J. Phys.: Condens. Matter **27**(5), 053202 (2015).
[22]A. Shakouri, "Recent developments in semiconductor thermoelectric physics and materials," Annu. Rev. Mater. Res. **41**(1), 399–431 (2011).
[23]J.-B.-J. Fourier, *Théorie Analytique de la Chaleur* (Firmin Didot, Paris, 1822).
[24]C. Cattaneo, "Sur une forme de i'equation de la chaleur eliminant le paradoxe d'une propagation instantanee (A form of heat conduction equation which eliminates the paradox of instantaneous propagation)," Comptes Rendus **247**, 431–433 (1958).
[25]P. Vernotte, "Les paradoxes de la theorie continue de l'équation de la chaleur," Comput. Rendus **246**, 3154–3155 (1958).
[26]D. Y. Tzou, "A unified field approach for heat conduction from macro- to micro-scales," J. Heat Transfer **117**(1), 8 (1995).
[27]R. A. Guyer and J. A. Krumhansl, "Solution of the linearized phonon Boltzmann equation," Phys. Rev. **148**(2), 766–778 (1966).
[28]R. A. Guyer and J. A. Krumhansl, "Thermal conductivity, second sound, and phonon hydrodynamic phenomena in nonmetallic crystals," Phys. Rev. **148**(2), 778–788 (1966).
[29]X. Li and S. Lee, "Role of hydrodynamic viscosity on phonon transport in suspended graphene," Phys. Rev. B **97**(9), 094309 (2018).
[30]X. Li and S. Lee, "Crossover of ballistic, hydrodynamic, and diffusive phonon transport in suspended graphene," Phys. Rev. B **99**(8), 085202 (2019).
[31]C. Liu, P. Lu, W. Chen, Y. Zhao, and Y. Chen, "Phonon transport in graphene based materials," Phys. Chem. Chem. Phys. **23**(46), 26030–26060 (2021).
[32]S. Berber, Y.-K. Kwon, and D. Tománek, "Unusually high thermal conductivity of carbon nanotubes," Phys. Rev. Lett. **84**(20), 4613–4616 (2000).
[33]S. Maruyama, "A molecular dynamics simulation of heat conduction in finite length SWNTs," Physica B **323**(1–4), 193–195 (2002).
[34]S. Maruyama, "A molecular dynamics simulation of heat conduction of a finite length single-walled carbon nanotube," Microscale Thermophys. Eng. **7**(1), 41–50 (2003).
[35]R. A. Escobar and C. H. Amon, "Thin film phonon heat conduction by the dispersion lattice Boltzmann method," J. Heat Transfer **130**(9), 1–8 (2008).
[36]A. Henry and G. Chen, "High thermal conductivity of single polyethylene chains using molecular dynamics simulations," Phys. Rev. Lett. **101**(23), 235502 (2008).
[37]A. Henry, G. Chen, S. J. Plimpton, and A. Thompson, "1D-to-3D transition of phonon heat conduction in polyethylene using molecular dynamics simulations," Phys. Rev. B **82**(14), 144308 (2010).
[38]S. Shen, A. Henry, J. Tong, R. Zheng, and G. Chen, "Polyethylene nanofibres with very high thermal conductivities," Nat. Nanotechnol. **5**(4), 251–255 (2010).
[39]N. Yang, G. Zhang, and B. Li, "Violation of Fourier's law and anomalous heat diffusion in silicon nanowires," Nano Today **5**(2), 85–90 (2010).
[40]Q. Liao, L. Zeng, Z. Liu, and W. Liu, "Tailoring thermal conductivity of single-stranded carbon-chain polymers through atomic mass modification," Sci. Rep. **6**(1), 34999 (2016).
[41]C. Huang, X. Qian, and R. Yang, "Thermal conductivity of polymers and polymer nanocomposites," Mater. Sci. Eng. R Rep. **132**, 1–22 (2018).
[42]A. Chen *et al.*, "High thermal conductivity polymer chains with reactive groups: A step towards true application," Mater. Adv. **1**(6), 1996–2002 (2020).
[43]M.-X. Zhu, H.-G. Song, Q.-C. Yu, J.-M. Chen, and H.-Y. Zhang, "Machine-learning-driven discovery of polymers molecular structures with high thermal conductivity," Int. J. Heat Mass Transfer **162**, 120381 (2020).
[44]X. Pan, M. G. Debije, and A. P. H. J. Schenning, "High thermal conductivity in anisotropic aligned polymeric materials," ACS Appl. Polym. Mater. **3**(2), 578–587 (2021).

[45]S.-M. Lee, D. G. Cahill, and R. Venkatasubramanian, "Thermal conductivity of Si–Ge superlattices," Appl. Phys. Lett. **70**(22), 2957–2959 (1997).
[46]G. Chen, "Thermal conductivity and ballistic-phonon transport in the cross-plane direction of superlattices," Phys. Rev. B **57**(23), 14958–14973 (1998).
[47]R. Yang and G. Chen, "Thermal conductivity modeling of periodic two-dimensional nanocomposites," Phys. Rev. B **69**(19), 195316 (2004).
[48]W. Lv and A. Henry, "Examining the validity of the phonon gas model in amorphous materials," Sci. Rep. **6**(1), 37675 (2016).
[49]W. Zhou, Y. Cheng, K. Chen, G. Xie, T. Wang, and G. Zhang, "Thermal conductivity of amorphous materials," Adv. Funct. Mater. **30**(8), 1903829 (2020).
[50]L. Lindsay, D. A. Broido, and T. L. Reinecke, "Thermal conductivity and large isotope effect in GaN from first principles," Phys. Rev. Lett. **109**(9), 095901 (2012).
[51]L. Lindsay, D. A. Broido, and T. L. Reinecke, "*Ab initio* thermal transport in compound semiconductors," Phys. Rev. B **87**(16), 165201 (2013).
[52]M.-Y. Shang, C. Zhang, Z. Guo, and J.-T. Lü, "Heat vortex in hydrodynamic phonon transport of two-dimensional materials," Sci. Rep. **10**(1), 8272 (2020).
[53]M.-Y. Shang, W.-H. Mao, N. Yang, B. Li, and J.-T. Lü, "Unified theory of second sound in two-dimensional materials," Phys. Rev. B **105**(16), 165423 (2022).
[54]N. Yang, G. Zhang, and B. Li, "Thermal rectification in asymmetric graphene ribbons," Appl. Phys. Lett. **95**(3), 033107 (2009).
[55]A. J. Minnich *et al.*, "Modeling study of thermoelectric SiGe nanocomposites," Phys. Rev. B **80**(15), 155327 (2009).
[56]Y. Hu, L. Zeng, A. J. Minnich, M. S. Dresselhaus, and G. Chen, "Spectral mapping of thermal conductivity through nanoscale ballistic transport," Nat. Nanotechnol. **10**(8), 701–706 (2015).
[57]S. Lee, X. Li, and R. Guo, "Thermal resistance by transition between collective and non-collective phonon flows in graphitic materials," Nanoscale Microscale Thermophys. Eng. **23**(3), 247–258 (2019).
[58]A. Sood *et al.*, "Quasi-ballistic thermal transport across MoS_2 thin films," Nano Lett. **19**(4), 2434–2442 (2019).
[59]D. Bagchi and P. K. Mohanty, "A microscopic model of ballistic-diffusive crossover," J. Stat. Mech. Theory Exp. **2014**(11), P11025 (2014).
[60]Y. Jing, M. Hu, and L. Guo, "Thermal conductivity of hybrid graphene/silicon heterostructures," J. Appl. Phys. **114**(15), 153518 (2013).
[61]J. Lee, J. Lim, and P. Yang, "Ballistic phonon transport in Holey silicon," Nano Lett. **15**(5), 3273–3279 (2015).
[62]F. Yang and C. Dames, "Mean free path spectra as a tool to understand thermal conductivity in bulk and nanostructures," Phys. Rev. B **87**(3), 035437 (2013).
[63]A. Majumdar and P. Reddy, "Role of electron–phonon coupling in thermal conductance of metal–nonmetal interfaces," Appl. Phys. Lett. **84**(23), 4768–4770 (2004).
[64]J. Cuffe *et al.*, "Reconstructing phonon mean-free-path contributions to thermal conductivity using nanoscale membranes," Phys. Rev. B **91**(24), 245423 (2015).
[65]J. Maassen and M. Lundstrom, "Steady-state heat transport: Ballistic-to-diffusive with Fourier's law," J. Appl. Phys. **117**(3), 035104 (2015).
[66]J. Maassen and M. Lundstrom, "A simple Boltzmann transport equation for ballistic to diffusive transient heat transport," J. Appl. Phys. **117**(13), 135102 (2015).
[67]J. Maassen and V. Askarpour, "Phonon transport across a Si–Ge interface: The role of inelastic bulk scattering," APL Mater. **7**(1), 013203 (2019).
[68]Y. Guo and M. Wang, "Phonon hydrodynamics for nanoscale heat transport at ordinary temperatures," Phys. Rev. B **97**(3), 035421 (2018).
[69]T. Luo, J. Garg, J. Shiomi, K. Esfarjani, and G. Chen, "Gallium arsenide thermal conductivity and optical phonon relaxation times from first-principles calculations," Europhys. Lett. **101**(1), 16001 (2013).
[70]D. Donadio and G. Galli, "Atomistic simulations of heat transport in silicon nanowires," Phys. Rev. Lett. **102**(19), 195901 (2009).
[71]P. K. Schelling, S. R. Phillpot, and P. Keblinski, "Comparison of atomic-level simulation methods for computing thermal conductivity," Phys. Rev. B **65**(14), 144306 (2002).
[72]A. J. H. McGaughey and M. Kaviany, "Phonon transport in molecular dynamics simulations: Formulation and thermal conductivity prediction," Adv. Heat Transfer **39**(06), 169–255 (2006).
[73]J.-P. M. Péraud and N. G. Hadjiconstantinou, "Efficient simulation of multidimensional phonon transport using energy-based variance-reduced Monte Carlo formulations," Phys. Rev. B **84**(20), 205331 (2011).
[74]J.-P. M. Péraud and N. G. Hadjiconstantinou, "An alternative approach to efficient simulation of micro/nanoscale phonon transport," Appl. Phys. Lett. **101**(15), 153114 (2012).
[75]V. Jean, S. Fumeron, K. Termentzidis, X. Zianni, and D. Lacroix, "Monte Carlo simulations of phonon transport in Si nanowires with constrictions," Int. J. Heat Mass Transfer **86**, 648–655 (2015).
[76]Z. Shomali, B. Pedar, J. Ghazanfarian, and A. Abbassi, "Monte-Carlo parallel simulation of phonon transport for 3D silicon nano-devices," Int. J. Therm. Sci. **114**, 139–154 (2017).
[77]Y. Guo and M. Wang, "Heat transport in two-dimensional materials by directly solving the phonon Boltzmann equation under Callaway's dual relaxation model," Phys. Rev. B **96**(13), 134312 (2017).
[78]S. Kumar, A. Majumdar, and C. L. Tien, "The differential-discrete-ordinate method for solutions of the equation of radiative transfer," J. Heat Transfer **112**(2), 424–429 (1990).
[79]J. Callaway, "Model for lattice thermal conductivity at low temperatures," Phys. Rev. **113**(4), 1046–1051 (1959).
[80]R. A. Guyer, "Phonon gas: A lattice Boltzmann description," Phys. Rev. E **50**(6), 4596–4608 (1994).
[81]W.-S. Jiaung and J.-R. Ho, "Lattice Boltzmann study on size effect with geometrical bending on phonon heat conduction in a nanoduct," J. Appl. Phys. **95**(3), 958–966 (2004).
[82]W.-S. Jiaung and J.-R. Ho, "Lattice-Boltzmann modeling of phonon hydrodynamics," Phys. Rev. E **77**(6), 066710 (2008).
[83]J. Lee, A. K. Roy, and B. L. Farmer, "Kapitza resistance in the lattice Boltzmann-Peierls-Callaway equation for multiphase phonon gases," Phys. Rev. E **83**(5), 056706 (2011).
[84]J. Lee, S. Sihn, A. K. Roy, and B. L. Farmer, "The lattice Boltzmann Peierls Callaway equation for mesoscopic thermal transport modeling," Int. J. Smart Nano Mater. **3**(1), 47–63 (2012).
[85]A. K. Roy, B. L. Farmer, V. Varshney, S. Sihn, J. Lee, and S. Ganguli, "Importance of interfaces in governing thermal transport in composite materials: Modeling and experimental perspectives," ACS Appl. Mater. Interfaces **4**(2), 545–563 (2012).
[86]Y. Guo and M. Wang, "Lattice Boltzmann modeling of phonon transport," J. Comput. Phys. **315**, 1–15 (2016).
[87]G. Qin *et al.*, "Resonant bonding driven giant phonon anharmonicity and low thermal conductivity of phosphorene," Phys. Rev. B **94**(16), 165445 (2016).
[88]G. Amati, S. Succi, and R. Piva, "Massively parallel lattice-Boltzmann simulation of turbulent channel flow," Int. J. Mod. Phys. C **08**(04), 869–877 (1997).
[89]S. Srinivasan, R. S. Miller, and E. Marotta, "Parallel computation of the Boltzmann transport equation for microscale heat transfer in multilayered thin films," Numer. Heat Transfer, Part B **46**(1), 31–58 (2004).
[90]W. Li, J. Carrete, N. A. Katcho, and N. Mingo, "ShengBTE: A solver of the Boltzmann transport equation for phonons," Comput. Phys. Commun. **185**(6), 1747–1758 (2014).
[91]J. Tan, T. R. Sinno, and S. L. Diamond, "A parallel fluid–solid coupling model using LAMMPS and Palabos based on the immersed boundary method," J. Comput. Sci. **25**, 89–100 (2018).
[92]J. Latt *et al.*, "Palabos: Parallel lattice Boltzmann solver," Comput. Math. Appl. **81**, 334–350 (2021).
[93]G. Chen, "Ballistic-diffusive heat-conduction equations," Phys. Rev. Lett. **86**(11), 2297–2300 (2001).
[94]S. I. Anisimov, B. L. Kapeliovich, and T. L. Perelman, "Electron emission from metal surfaces exposed to ultrashort laser pulses," J. Exp. Theor. Phys. **39**(2), 375–377 (1974) [Zh. Eksp. Teor. Fiz. **66**, 776–781 (1974)].

[95]T. Q. Qiu and C. L. Tien, "Short-pulse laser heating on metals," Int. J. Heat Mass Transfer. **35**(3), 719–726 (1992).
[96]S. Kumar and K. Mitra, "Microscale aspects of thermal radiation transport and laser applications," Adv. Heat Transfer **33**, 187–294 (1999).
[97]A. K. Upadhyay, N. A. Inogamov, B. Rethfeld, and H. M. Urbassek, "Ablation by ultrashort laser pulses: Atomistic and thermodynamic analysis of the processes at the ablation threshold," Phys. Rev. B **78**(4), 045437 (2008).
[98]M. Olbrich, E. Punzel, P. Lickschat, S. Weißmantel, and A. Horn, "Investigation on the ablation of thin metal films with femtosecond to picosecond-pulsed laser radiation," Phys. Proc. **83**, 93–103 (2016).
[99]K.-C. Liu and Y.-S. Chen, "Analysis of heat transfer and burn damage in a laser irradiated living tissue with the generalized dual-phase-lag model," Int. J. Therm. Sci. **103**, 1–9 (2016).
[100]W. Kim *et al.*, "Thermal conductivity reduction and thermoelectric figure of merit increase by embedding nanoparticles in crystalline semiconductors," Phys. Rev. Lett. **96**(4), 045901 (2006).
[101]R. Escobar, B. Smith, and C. Amon, "Lattice Boltzmann modeling of sub-continuum energy transport in crystalline and amorphous microelectronic devices," J. Electron. Packag. **128**(2), 115–124 (2006).
[102]P. Zhang *et al.*, "Thermoelectric properties of four typical silicon allotropes," Model. Simul. Mater. Sci. Eng. **26**(8), 085006 (2018).
[103]L. Yang *et al.*, "Decoupling electron and phonon transport in single-nanowire hybrid materials for high-performance thermoelectrics," Sci. Adv. **7** (20), 18–20 (2021).
[104]R. A. Escobar, S. S. Ghai, M. S. Jhon, and C. H. Amon, "Multi-length and time scale thermal transport using the lattice Boltzmann method with application to electronics cooling," Int. J. Heat Mass Transfer **49**(1–2), 97–107 (2006).
[105]J. Ghazanfarian and Z. Shomali, "Investigation of dual-phase-lag heat conduction model in a nanoscale metal-oxide-semiconductor field-effect transistor," Int. J. Heat Mass Transfer **55**(21–22), 6231–6237 (2012).
[106]J. Gao, L. W. Wang, R. Z. Wang, and Z. S. Zhou, "Solution to the sorption hysteresis by novel compact composite multi-salt sorbents," Appl. Therm. Eng. **111**, 580–585 (2017).
[107]R. J. Warzoha *et al.*, "Applications and impacts of nanoscale thermal transport in electronics packaging," J. Electron. Packag. **143**(2), 0208041 (2021).
[108]H. D. Arnold and I. B. Crandall, "The thermophone as a precision source of sound," Phys. Rev. **10**(1), 22–38 (1917).
[109]E. C. Wente, "The thermophone," Phys. Rev. **19**(4), 333–345 (1922).
[110]R. Dutta *et al.*, "Gold nanowire thermophones," J. Phys. Chem. C **118**(50), 29101–29107 (2014).
[111]A. E. Aliev *et al.*, "Alternative nanostructures for thermophones," ACS Nano **9**(5), 4743–4756 (2015).
[112]S. Julius, R. Gold, A. Kleiman, B. Leizeronok, and B. Cukurel, "Modeling and experimental demonstration of heat flux driven noise cancellation on source boundary," J. Sound Vib. **434**, 442–455 (2018).
[113]S. A. Romanov, A. E. Aliev, B. V. Fine, A. S. Anisimov, and A. G. Nasibulin, "Highly efficient thermophones based on freestanding single-walled carbon nanotube films," Nanoscale Horiz. **4**(5), 1158–1163 (2019).
[114]B. Leizeronok, S. Losin, A. Kleiman, S. Julius, I. Romm, and B. Cukurel, "Guidelines for higher efficiency supported thermo-acoustic emitters based on periodically Joule heated metallic films," J. Acoust. Soc. Am. **153**(3), 1682–1693 (2023).
[115]A. Sow, S. Losin, B. Leizeronok, A. Kleiman, and B. Cukurel, "Application of embedded thermophones toward tonal noise cancelation in small-scale ducted Fan," J. Vib. Acoust. **147**(2), 021006 (2025).
[116]S. S. Ghai, W. T. Kim, R. A. Escobar, C. H. Amon, and M. S. Jhon, "A novel heat transfer model and its application to information storage systems," J. Appl. Phys. **97**(10), 10P703 (2005).
[117]G. Qin, H. Wang, L. Zhang, Z. Qin, and M. Hu, "Giant effect of spin–lattice coupling on the thermal transport in two-dimensional ferromagnetic CrI_3," J. Mater. Chem. C **8**(10), 3520–3526 (2020).
[118]J. P. McKelvey, R. L. Longini, and T. P. Brody, "Alternative approach to the solution of added carrier transport problems in semiconductors," Phys. Rev. **123**(1), 51–57 (1961).
[119]J. P. McKelvey and J. C. Balogh, "Flux methods for the analysis of transport problems in semiconductors in the presence of electric fields," Phys. Rev. **137** (5A), A1555–A1561 (1965).
[120]W. Shockley, "Diffusion and drift of minority carriers in semiconductors for comparable capture and scattering mean free paths," Phys. Rev. **125**(5), 1570–1576 (1962).
[121]J.-H. Rhew and M. S. Lundstrom, "Drift-diffusion equation for ballistic transport in nanoscale metal-oxide-semiconductor field effect transistors," J. Appl. Phys. **92**(9), 5196–5202 (2002).
[122]C. Jeong, R. Kim, M. Luisier, S. Datta, and M. Lundstrom, "On Landauer versus Boltzmann and full band versus effective mass evaluation of thermoelectric transport coefficients," J. Appl. Phys. **107**(2), 023707 (2010).
[123]A. J. C. Ladd, "Modeling, Theory, and Simulation," Ladd Research Group, University of Florida Department of Chemical Engineering, https://che.ufl.edu/research/modeling-theory-and-simulation/name/anthony-ladd (accessed 14 July 2026).